Chapter II Experimental Details of the Molecular Beam, Liquid Surfaces, and Spectroscopic Detection

2.1 Introduction

Experimental studies of gas-liquid scattering dynamics involve a molecular beam that strikes a refreshed liquid surface where translational and internal state distributions of the scattered gas are measured with a Pb-salt diode laser spectrometer. Throughout this thesis, important details of the specific experimental conditions are listed in each chapter to help understand the measurements. To complement these descriptions, additional information of the components are outlined and discussed in this chapter for the general experimental setup that is illustrated in Figure 2.1. The objective to understand the energy transfer dynamics involves measuring the change between initial and final states of the CO_2 projectile. Based on this scheme, the scattering experiments necessitate a thorough characterization of the molecular beam and liquid surface to quantify the initial state of the system. These preliminary studies also are used to show that the final distributions reflect nascent collision conditions between the gas and liquid surface.

In these studies, skimmed molecular beams are employed in an effort to (i) control the incident energy, (ii) reduce the angular spread, and (iii) limit the temperature of the internal state distribution.[1] These projectiles are scattered from low vapor pressure liquids in a chamber under high vacuum where the flux is measured with a high resolution infrared laser. The liquids are prepared via methods

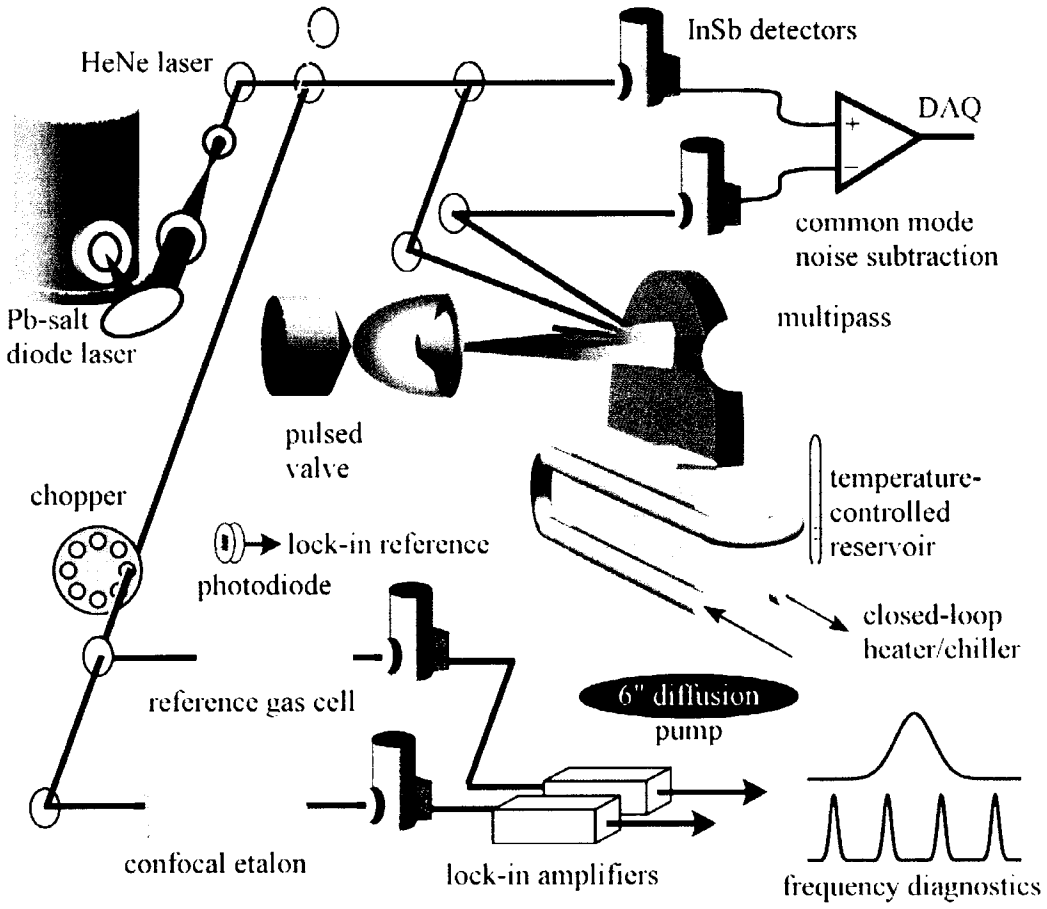

Figure 2.1 Schematic of the Pb-salt diode laser spectrometer used to detect CO_2 in the gas-liquid scattering experiments.

that ensure the liquid target is clean and freshly renewed.[2] The laser detects the scattered CO_2 1–2 cm from the surface, which imposes an important condition on the choice of incident flux and liquid surface. Specifically, the mean free path for CO_2 in the chamber should be at least an order of magnitude larger than the surface-to-laser distance to guarantee the measured distributions reflect only the dynamics of the gas-liquid interaction. Such a requirement limits the incident flux, background pressures, and vapor pressure of the liquid. The versatility of high resolution diode laser enables

us to characterize the translation, rotation, vibration, and M_J-states of the scattered CO_2. Important aspects about the laser diode spectrometer, molecular beam, and liquid surface preparation are covered to illustrate the initial characterization of the system. In addition, the computer-controlled interface and data analysis are described in detail.

2.2 Laser Detection Scheme

2.2.1 Pb-salt Diode Laser

As illustrated in Figure 2.1, the infrared spectrometer is built around a tunable single mode Pb-salt diode laser. The diode generates light that is tunable around λ = 4.2 μm, which is used to detect incident and scattered CO_2 through direct Beer's Law absorption. Important features of the diode include single mode lasing, low amplitude noise, and narrow line width ($\Delta\nu_{laser} \approx 20$ MHz) to accurately determine the internal state populations of the Doppler broadened absorption profiles. Details of the laser physics are extensively covered in expert reviews and texts, while the specific operating characteristics have been presented in previous JILA theses.[3,4] Based on the collection of previous work, this section provides a brief overview of the diode laser, as well as specifics about its use in the gas-liquid scattering experiments.

The diode laser is an optical oscillator that incorporates both the gain medium and optical cavity inside a semiconductor with cleaved ends. The construction of the laser is based on lead salts that are doped with impurities from groups III and V on the periodic table. Figure 2.2 illustrates the physical and chemical components of the

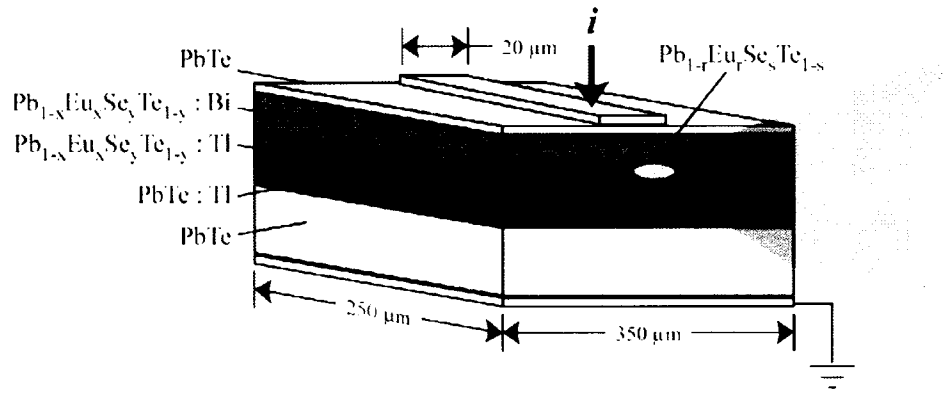

Figure 2.2 Heterojunction Pb-salt diode laser.

heterojunction laser, which has been constructed from molecular beam epitaxy (MBE) to precisely control the thickness of the different layers in the diode.[3] In general, the Pb-salt diode behaves as a typical semiconductor where the electronic structure includes valance (VB) and conduction bands (CB) for the electrons (e^-).[5] Electrons within these bands are distributed based on energy by a Boltzmann factor that incorporates a temperature. At 300 K, the energy difference between the VB and CB results in a distribution where the vast majority of electrons reside in the valance band. These electrons may be excited into the conduction band if the semiconductor absorbs a photon with an energy greater than the band gap, ($E_{gap} = E_{CB} - E_{VB}$), which leads to a positive hole (h^+) in the valance band. The physical process is illustrated in Figure 2.3a to show a transition, for which energy and momentum (k) are conserved, i.e. a vertical with respect to k. Once the e^-–h^+ pair is created, dynamics in the semiconductor may lead to recombination through either radiative or nonradiative pathways.

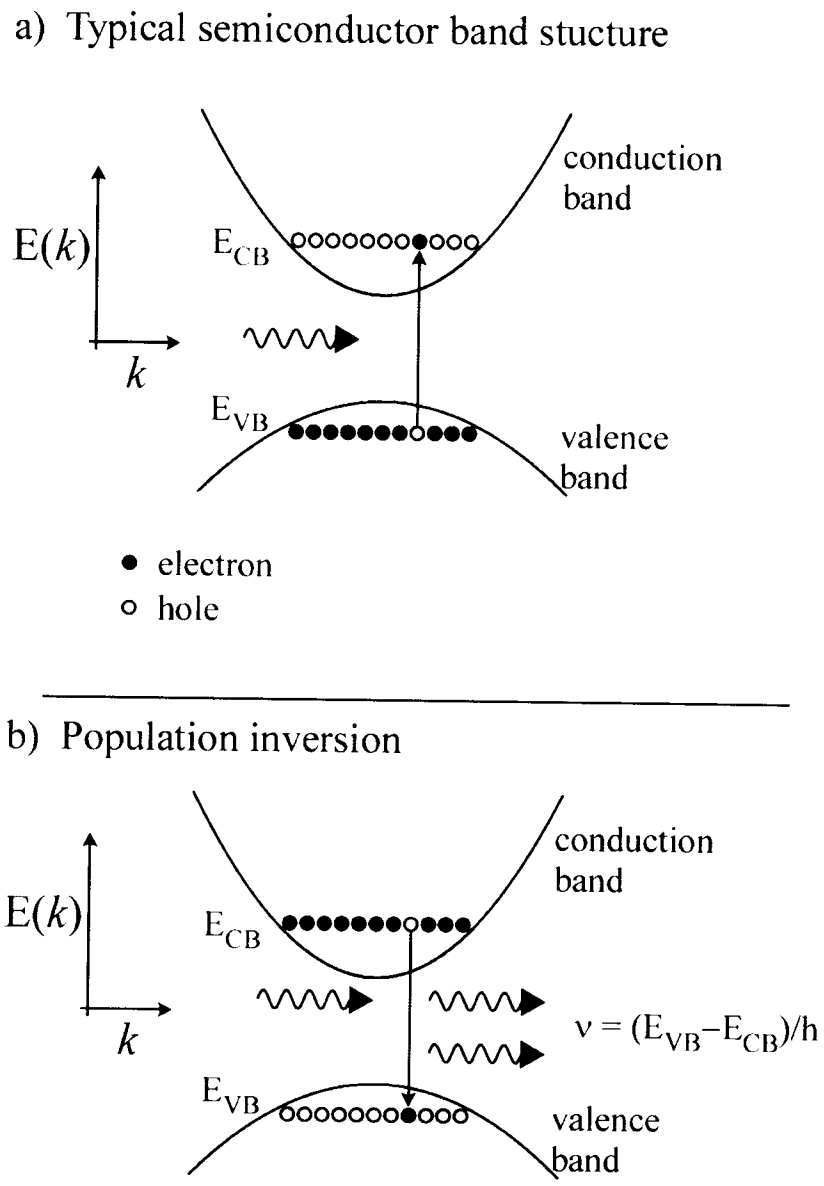

Figure 2.3 Electronic structure of a semiconductor. (a) Energy versus momentum for a typical semiconductor that absorbs a photon to promote an electron from the valance to conduction band. (b) Population inversion leads to radiative recombination to generate lasing in the diode.

To utilize these properties for lasing, the Pb-salt diode is grown with an active region that is defined by the *p-n* junction. Figure 2.2 shows that the Pb salts in the diode have been doped with either Tl (*p*-type) or Bi (*n*-type). These impurities lead to crystal sites that either have one too many (*n*) or too few (*p*) electrons to bond with the semiconductor lattice. The extra electron from the *n*-type impurity easily reaches the conduction band through thermal excitation, at which point it may diffuse and recombine with a hole in a *p*-type impurity. As a result, positive and negative charges develop as the electrons and holes diffuse across the junction. The process stops when the voltage drop across this depletion region is large enough to prevent further diffusion of e^- and h^+. To generate a population inversion, an external voltage is applied across the *p-n* junction to counter the inherent potential difference across the depletion region. Once the diode is forward biased in this way, electrons flow through the conduction band to create the necessary population inversion. These electrons may recombine with holes in the valance band to emit a photon as they are forced into the same physical region of the diode. The process is illustrated in Figure 2.3b for a general population inversion in the semiconductor. Constant current injection into the active region maintains the population inversion that lead to continuous (cw) lasing.

In addition to the gain medium, the optical cavity of the laser is formed by cleaving the ends of the semiconductor to utilize the properties of Fresnel reflection. The index of refraction in the diodes is ≈ 5 at $\lambda = 4.2$ μm, which leads to cavity mirrors that are $\approx 44\%$ reflective. As illustrated in Figure 2.2, the physical length of the active region is ≈ 250 μm, which corresponds to a free spectral range (FSR) of ≈ 4

cm^{-1} for the cavity. The diode begins lasing when the round trip gain in the cavity exceeds the losses, which include photons that are lost to reabsorption by the semiconductor, transmission through the cleaved ends, or pathways out of the active region. In addition, lasing competes with nonradiative pathways that involve recombination at lattice defect sites and Auger processes. Sustained lasing requires increasing the injection current to the point where the radiative recombination leads to stimulated emission in the cavity. The specific currents to reach lasing threshold depend upon the temperature of the diode. For example, the threshold rises from 110 mA at 81 K to 203 mA at 111 K for the Pb-salt diode used in the CO_2 experiments. In general, the threshold current increases with temperature because losses due to Auger recombination processes tend to increase with temperature as well.

2.2.2 Laser Tuning

The laser used in the CO_2 scattering studies is part of a spectroscopic system developed by a company once known as Laser Photonics, which is now Laser Components. The laser is a heterojunction diode (model L5622-2100, serial no. 87-05) mounted on a cold finger inside a main liquid N_2-cooled dewar (L5736, position #3), which is fed by an auxiliary reservoir (L5737) to provide extended periods between refills. The frequency of light depends on the band gap of the semiconductor, which changes with temperature at a rate of 3–4 cm^{-1}/K. This feature of the diode laser requires a controller that provides a dynamic range to access many temperatures and long time stability for scanning purposes. The temperature inside the dewar is regulated through resistive heating tape (13 Ω) that is firmly secured to the base of the main reservoir. Two silicon diodes are also attached to this cold finger

to provide a feedback reference to the temperature controller (Laser Photonics, SP5720). The voltage drop across the diodes is measured and compared to the set point voltage on the controller. The actual voltages correspond to a particular temperature through a calibration curve listed in Table 2.1. Servo loop electronics steady the temperature to within 0.1 mK so that the drift over the course of a scan (≈ 1 min) is negligible.

In addition to stability, the controller provides enough current to resistively heat the diode to ≈ 180 K. The base temperature is determined by the quality of vacuum in the insulating walls of the dewar, which is periodically evacuated to remove condensed gas that leaks into the chamber. Instead of a restoration to room temperature, a partial warming routine is typically employed to help maintain the mapped-out mode structure of the laser. To do this, the vacuum port is connected to a LN_2 trapped diffusion pump, at which point the temperature controller is set to bring the dewar to 180 K (T_{dewar} = 0.6900 V) to help release gases such as nitrogen, oxygen, argon and CO_2. After ~ 1–3 hours of pumping, the valves are closed, the heater is turned off, and the dewar is allowed to cool back to LN_2 temperatures. Base temperatures typically reach 80–81 K with this procedure.

The injection current also determines the frequency of the diode laser. The process is based on the response of the index of refraction to the local charge density in the active region of the semiconductor. The index of refraction increases with current, which effectively lengthens the laser cavity. As a result, the diode may be continuously tuned with a modulated current at a rate of ≈ 2 MHz/μA. The controller is a commercial unit from ILX Lightwave (LDX-3620), which is designed to be an

Table 2.1 Diode laser dewar temperature calibration.

Voltage	T (K)	Voltage	T (K)	Voltage	T (K)
0.9797	70	0.9357	89	0.8972	104
0.9643	77	0.9332	90	0.8921	106
0.9620	78	0.9307	91	0.8871	108
0.9597	79	0.9281	92	0.8821	110
0.9574	80	0.9256	93	0.8770	112
0.9550	81	0.9230	94	0.8719	114
0.9527	82	0.9204	95	0.8669	116
0.9503	83	0.9178	96	0.8618	118
0.9479	84	0.9152	97	0.8567	120
0.9455	85	0.9125	98	0.8312	130
0.9431	86	0.9099	99	0.8054	140
0.9406	87	0.9072	100	0.7795	150
0.9382	88	0.9022	102	0.3664	298

ultra low noise current supply. This is important because any current noise on the source corresponds to additional line width broadening based on the tuning rate of the laser. For example, the specifications from ILX claim that the current noise should be < 2 μA RMS in a 10 kHz bandwidth, which would correspond to an additional 4-5 MHz of broadening beyond the inherent line width of the laser. These noise sources are carefully analyzed with simple diagnostics that involve passing the output of the current controller through a 10 Ω resistor to generate a voltage, which is sent to a spectrum analyzer. Adapters have been made to attach at various points along the cable layout to help identify any additional sources of noise. A sample noise spectrum is plotted in Figure 2.4 to assess the difference between the high and low band width settings. In addition, detailed analysis shows that the noise amplitude

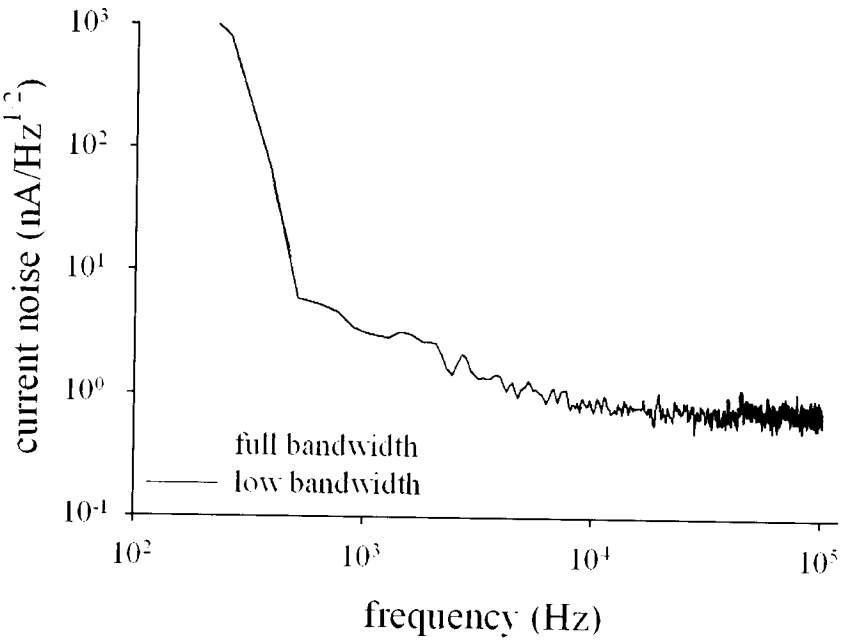

Figure 2.4 Spectral noise density of diode laser current controller.

over all frequencies is 2–3 times lower for the 200 mA versus 500 mA setting. Such a result clearly indicates the modulation circuitry contributes to the noise on the output. Additional features in the spectrum include a peak at 100 kHz that corresponds to the vibrational frequency of a quartz oscillator used in the A/D for the digital display. These effects have been minimized through an external modification where the oscillator is isolated from the circuit board with an on-off switch. Such a feature once again illustrates the limitations of the ILX design. Current efforts in the JILA electronics shop have produced current sources with noise floors one to three orders of magnitude lower than the best ILX drivers.

The procedure to scan the diode laser across a rovibrational transition involves several steps. First, the temperature is set and allowed to stabilize, at which point the current is tuned to the general vicinity of the transition. Once the absorption feature has been identified on the scope trace of the reference gas cell, the current is slowly decreased so that the starting point of the scan is shifted 500–1000 MHz below the centerline transition frequency. The data acquisition software provides an output voltage to the current controller that is incrementally increased to scan the laser after every gas pulse. This voltage output first passes through the ground loop breaker and low pass filter that is illustrated in Figure 2.5 with the ILX current controller set to the DC MOD position. Further details of this routine are outlined in the comments within the source code in of the scanning program listed in Appendix D.

The diode laser covers ≈ 90% of the frequencies between 2293 and 2375 cm^{-1} with light powers that range from ≈ 0.1 – 2 μW depending on the temperature and injection current. Various combinations of temperatures and currents are used to access the majority of these frequencies. Generally, the laser covers ≈ 1 cm^{-1} in a single longitudinal mode before the gain curve shifts and the frequency jumps ahead by one FSR of the cavity. Sample tuning curves are plotted in Figure 2.5 to show the frequency coverage as a function of current for two temperatures. Spectral maps are generated every time the diode is temperature cycled, which tends to restructure the semiconductor band structure by small amounts. The characterization involves sweeping the laser with a saw-tooth wave from a function generator so that signals from the reference gas cell and etalon are visible on an oscilloscope. Transitions are

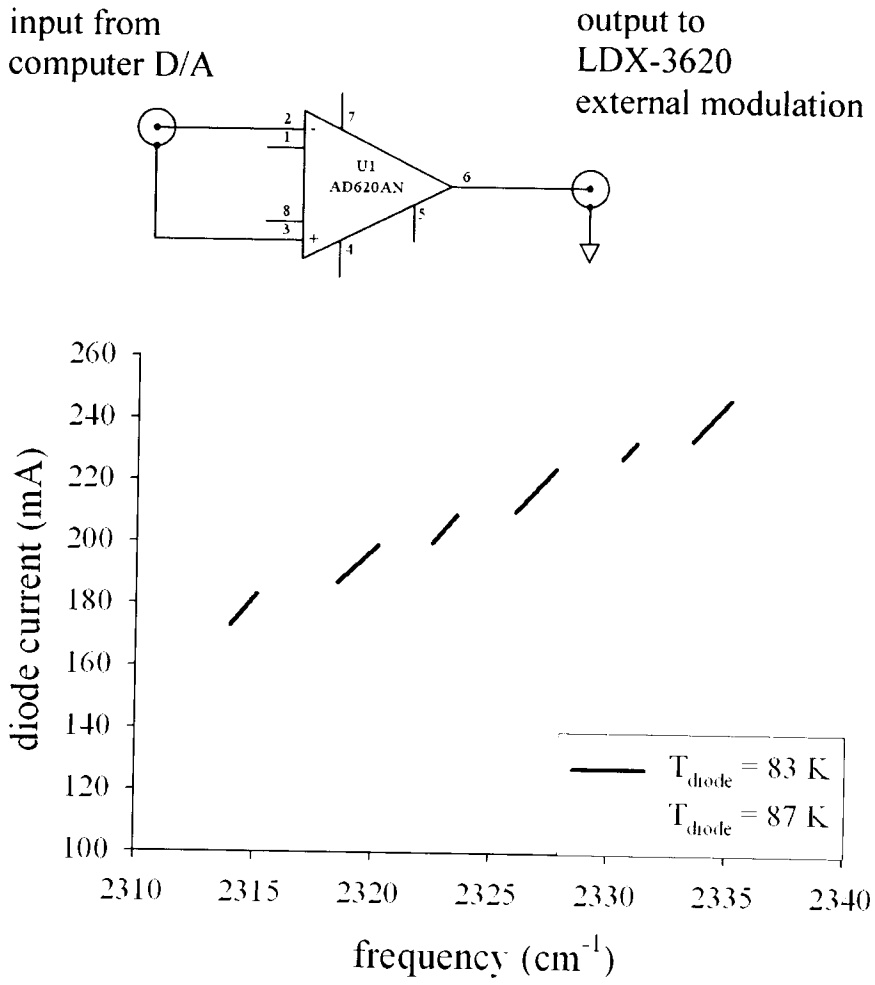

Figure 2.5 Spectral coverage of diode laser. A simple differential amplifier is used to electronically isolate the current controller from the computer interface.

recorded as a function of T(V) and *i* for rotational states in the ground (00^00) and degenerate excited state ($01^{1e/f}0$) vibrational manifold. Tables of temperatures, currents, and transitions are used to find the correct frequencies in the incident beam characterization and scattering experiments.[6,7]

As the diode laser scans across Doppler broadened absorption profiles in the experiment, the line shapes are best characterized by a convolution of Gaussian and

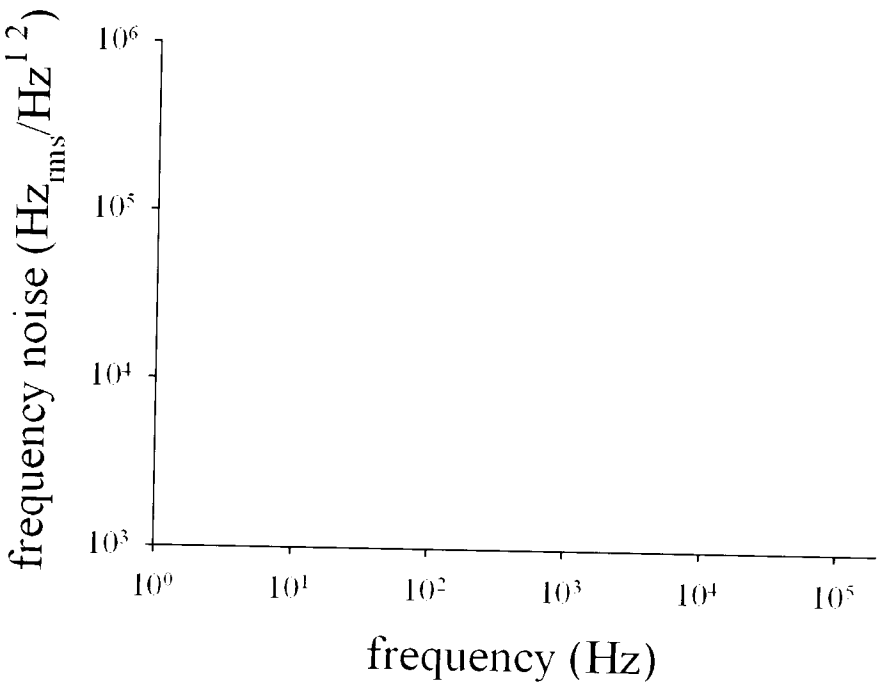

Figure 2.6 Frequency noise of Pb-salt diode laser.

Lorentzian components within a Voigt function. The Gaussian fraction corresponds to a velocity distribution within the gas sample, which is typically Maxwell-Boltzmann and defined by the temperature of the sample. Additional line shape broadening is due to the width of the laser ($\Delta\nu_{laser} \approx 20$ MHz), which are extracted from a least squares deconvolution of the two components. A simple test to confirm these values involves a frequency-to-amplitude transducer that converts frequency noise on the laser into amplitude noise. To do this, the laser is parked on the side of a CO_2 absorption, at which point peak-to-peak amplitude noise is recorded for the given laser power. The laser is then tuned off-resonance to determine the baseline noise level, which is subtracted from the first measurement in quadrature. This

amplitude noise (in absorbance) is converted to frequency noise through the slope at the side of the CO_2 absorption line shape, which provides a direct relationship between absorbance and frequency. These values reflect a broad-band characterization of the noise. To help understand the frequency components, the transducer signals are also recorded by a spectrum analyzer to reveal the noise density as a function of frequency. The noise spectral density for the CO_2 laser is illustrated in Figure 2.6.

2.2.3 Detectors

Infrared light detectors in the spectrometer are built from semiconductor materials similar to the construction of the laser diode. As depicted in Figure 2.3a, the detector element absorbs incident radiation where photons with $h\nu > E_{gap}$ excite electrons from the valance to the conduction band. This process is typically characterized by a quantum yield, which is the number of electron-hole pairs created per photon. Detectors made with materials such as InSb and HgCdTe have quantum yields that typically exceed 90%. Based on the properties of the semiconductor, these devices are combined with electronic amplifiers in one of two ways. The first type is photoconductive (PC) in which the excited electron in the conduction band decreases the impedance of the semiconductor. The second class of detectors is photovoltaic (PV), which is based on a *p-n* diode junction where photons excite electrons from the VB to the CB in the depletion region of the diode. These electrons are then accelerated by the bias voltage to create a photocurrent through the detector element. Both types of detectors provide an extremely sensitive way to monitor laser power for

a) InSb Photovoltaic Detector

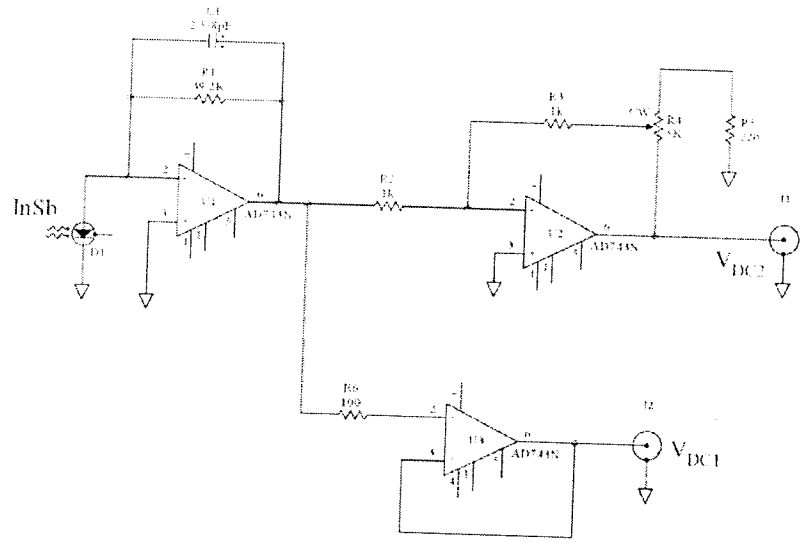

b) MCT Photoconductive Detector

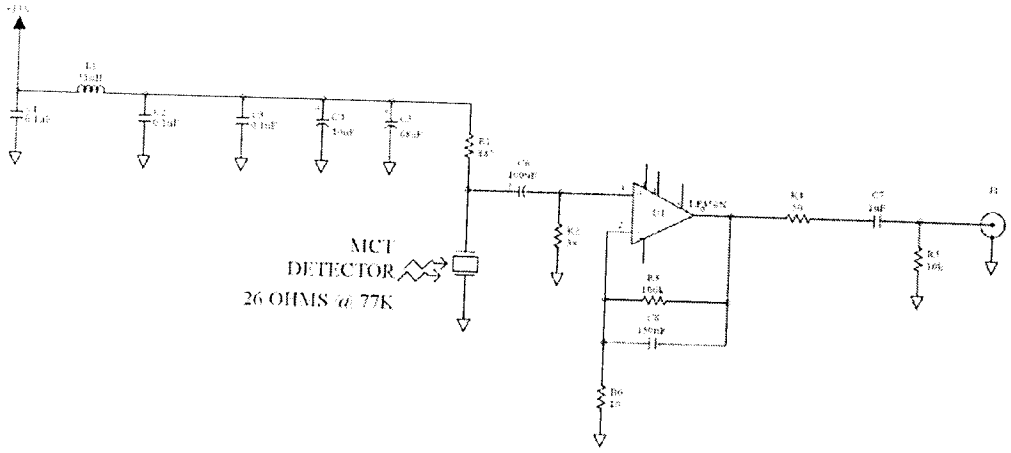

Figure 2.7 Electronic amplifier circuits for InSb photovoltaic and MCT photoconductive detectors.

the direct absorption experiments. As a result, each detector is fully characterized to determine sources of noise that may inhibit optimal performance.

The laser detection scheme includes splitting the light onto two detectors. The first path involves multiple passes through the vacuum chamber to measure the density of CO_2 in the scattered flux, while the second fraction is passed directly onto a reference detector. In this configuration, the signal and reference detectors are InSb photovoltaics (Infrared Associates, IS-0.5), for which the elements have been matched in an effort to generate identical amplitude and frequency responses within each detector circuit. The semiconductor is mounted in a liquid N_2 dewar that is built with sapphire windows and a 30° field-of-view (FOV) cold shield to reduce shot noise from incident blackbody radiation. The element itself is square with an area of 0.5×0.5 mm^2, which leads to an inherent capacitance of 20 pF across the InSb material. The photocurrent from the InSb passes into an amplifier circuit that is directly mounted to the back of the dewar in a side sealed compartment. The schematic is printed in Figure 2.7a to illustrate the two-stage amplification, which is based on an initial transimpedance of 39.4 kΩ. The photocurrent and transimpedance lead to a voltage drop across the first stage of the amplifier, where $V = iR$. The second stage of the amplifier provides adjustable gain from 1–30.2 that is controlled a potentiometer in the circuit. The low power from the diode laser requires the maximum amplification, so the potentiometer has been set so the gain is 30.2. In addition, a buffer is included to measure the voltage directly after the transimpedance amplifier. The gain of the second stage may be calculated directly from the ratio of the two voltage outputs on the circuit.

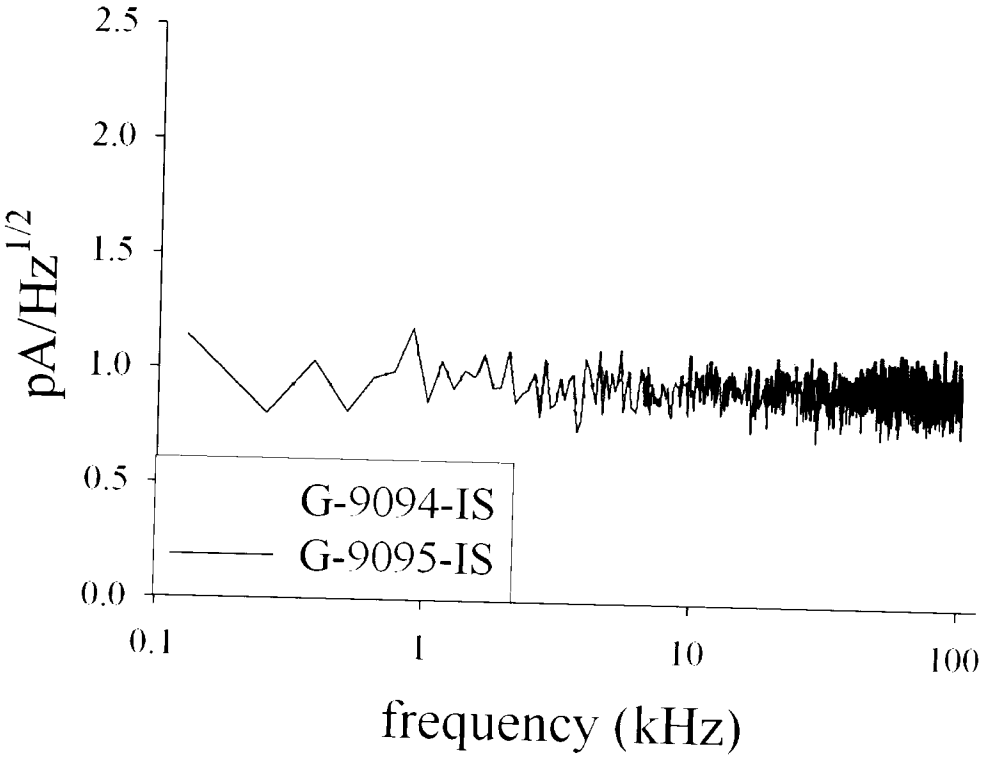

Figure 2.8 Current noise of signal and reference InSb detectors.

The sensitivity of these detectors is based on fundamental noise limitations of the individual components in the circuit. The contributions include (i) detector element noise, (ii) Johnson noise from the transimpedence resistor, (iii) amplifier noise, and (iv) shot noise from background blackbody radiation. These incoherent sources add together in quadrature to limit the overall performance of the detector, which is characterized with an FFT spectrum analyzer. The plot in Figure 2.8 shows the noise density of both detectors, where the measurement involves passing the

output voltage directly into the analyzer. The baseline current noise above 1 kHz is ≈ 0.9 pA/Hz$^{1/2}$ for both detectors, which corresponds to a voltage noise of 36.2 nV$_{rms}$/Hz$^{1/2}$ across the 39.4 kΩ transimpedence. To better understand the contributions to this noise level, we can investigate the magnitude of each component listed in the first part of this paragraph. First, the intrinsic noise on the detector element is not provided by the manufacturer, so the value is estimated from the noise measurements at the end of the analysis. Second, Johnson noise from the resistor is $V_{rms}/Hz^{1/2} = (4k_BTR)^{1/2}$, which leads to 25.7 nV$_{rms}$/Hz$^{1/2}$ for the 39.4 kΩ resistor at room temperature. Third, the amplifier (AD743N) includes both current and voltage noise sources, which are specified to be 6.9 fA$_{rms}$/Hz$^{1/2}$ and 2.9 nV$_{rms}$/Hz$^{1/2}$, respectively. The current noise adds an additional 0.28 nV$_{rms}$/Hz$^{1/2}$ across the transimpedence resistor, i.e. completely negligible when the sum of these sources are added in quadrature.

The final component is shot noise from the flux of photons due to room temperature background blackbody radiation. Shot noise contributions are governed by $i_{rms}/Hz^{1/2} = (2qi_{DC})^{1/2}$, which requires an estimate for the photocurrent from the blackbody photons. The flux density (photons/s/m^3) may be integrated over wavelengths that range from the visible to 5.5 μm, which is the spectral region where the InSb detector responds to light. Such a calculation reveals that the incident flux of photons is 2.6×10^{16} photons/s/cm^2, which corresponds to 6.6×10^{13} photons/s for a detector area of 0.5×0.5 mm^2. As previously mentioned, the FOV cold shield is designed to significantly reduce this incident flux by only exposing the detector to room temperature blackbody through a 30° solid angle. The FOV decreases the flux

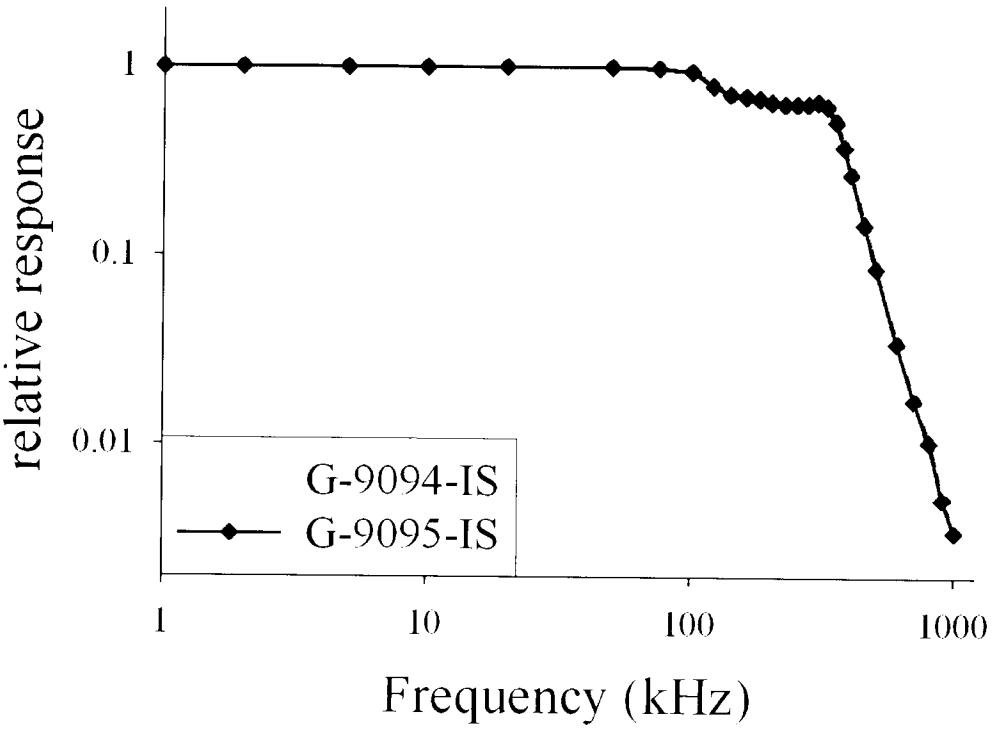

Figure 2.9 Frequency response of InSb detectors.

by a factor of 0.0334 to yield 2.21×10^{12} photons/s, which corresponds to 0.35 μA of photocurrent if the quantum yield is assumed to be near unity. Shot noise from this background current is 0.34 $pA_{rms}/Hz^{1/2}$, which leads to 13.3 $nV_{rms}/Hz^{1/2}$. Contributions from shot noise, Johnson noise, and the amplifier result in 29.1 $nV_{rms}/Hz^{1/2}$, which can be used to estimate the noise on the detector element. As a result, we estimate the detector noise to be 21.1 $nV_{rms}/Hz^{1/2}$, which is a factor of two better than the previous InSb detectors used in earlier versions of the Pb-salt diode laser spectrometer.

The detectors respond to changes in light levels on a time scale that correspond to the finite bandwidth created by the capacitance of the *p-n* junction and the transimpedence in the amplifier. The bandwidth is measured with a red LED that is controlled by a square wave from a function generator. These two components are tested with a silicon photodiode (FND-100) with a bandwidth of 700 kHz to ensure the frequency response of the testing equipment is adequate for the InSb characterization. The plot in Figure 2.9 shows the relative response of each detector at a series of frequencies that extend out to 500 kHz. From this plot, the bandwidth of these detectors is defined by the -3dB point, which falls at 150 kHz for the InSb circuit.

Infrared light in the frequency diagnostic arm of the spectrometer is detected with HgCdTe PC detectors, which are used to record the transmission fringes through the etalon and room temperature absorption profile in the reference gas cell. The MCT element is 1.0×1.0 mm^2 and is mounted behind a 30° FOV cold shield in a liquid N_2 cooled dewar. These semiconductors are sensitive to light with wavelengths that reach 12.5 μm. Signals are processed with the amplifier circuit printed in Figure 2.7b, which shows the output voltages are AC coupled. The voltages are sent to lock-in amplifiers where the signals are heterodyned against a reference signal. In general, the MCT elements are an order of magnitude less sensitive compared to the InSb materials. These particular detectors are worse due to previous damage or other general mishandling. Despite these limitations, laser powers that correspond to a fraction of μW on each detector are visible on the MCT

detectors. The sensitivity of the element + amplifier is significantly improved by the lock-in amplification scheme.

2.2.4 Spectrometer

Other than the laser and detectors, the spectrometer consists of additional optical components that are used to measure the scattered CO_2 flux and frequency of the laser. The entire spectrometer is built within a purge box built from ¼" sheets of plexiglass that is filled with dry N_2 to remove atmospheric CO_2 from the path of the laser beam. The infrastructure of the box includes aluminum posts, hinges, and clasps to keep the lids closed during experiments. Airtight seals are generated with weather stripping and electrical tape along the sealing surfaces. Polyflo tubing from a 1A tank of nitrogen is passed into the purge box to eliminate the presence of CO_2. In general, 1–2 full tanks are used for an incident beam + scattering experiment. The remaining parts of the spectrometer are constructed from stock and custom mirrors and lenses. Stock lenses are made from either BaF_2 or CaF_2, while the mirrors are gold on a base of chromium with Zerodur or fused silica substrates. These optics are available from Janos, Edmund Optics, or CVI. Further details about the custom pieces are provided throughout the description in the text.

The illustration in Figure 2.1 shows the ways in which the laser beam is split within the spectrometer to measure the scattered flux as a function of frequency. Before the beam is split, the light is carefully collimated with an off-axis parabola (OAP) (Janos, A8037-305, d = 3", f = 1.5") positioned directly in front of the laser output. The cartoon in Figure 2.10 shows the OAP on an *x y z* translation stage that is fixed to an adapter plate for coarse alignment on the laser table. This plate has ¼"

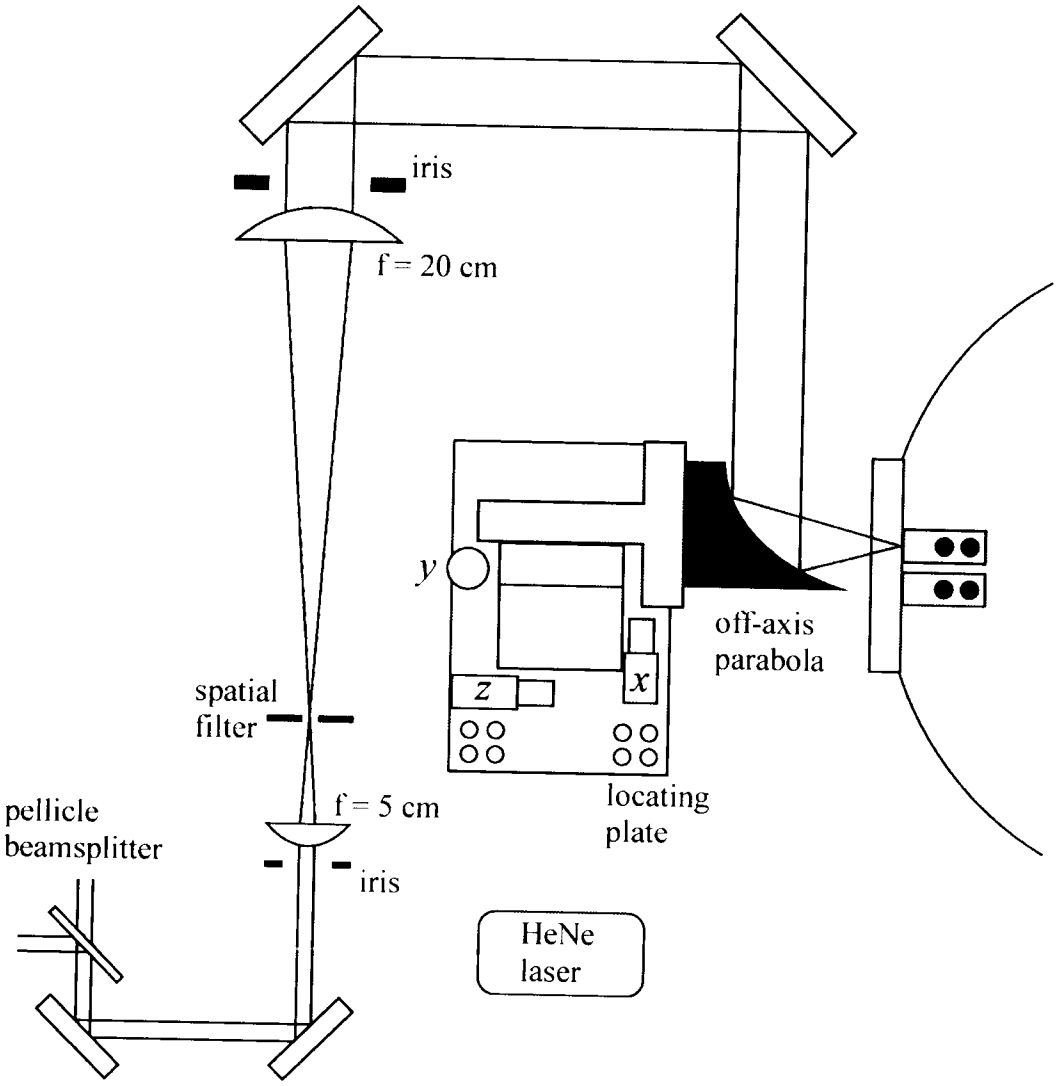

Figure 2.10 Laser collimation and telescope configuration. The diode laser light is first collimated with an off-axis parabola, after which it passes through a 4:1 reducing telescope. A pinhole aperture is used to spatially filter the beam. The IR beam is overlapped with a HeNe beam for alignment throughout the rest of the spectrometer.

thru holes positioned in a pattern that allows the OAP to be positioned anywhere with respect to the laser. To coarsely locate the OAP in front of the laser, a HeNe beam is aligned 4" off the laser table, and then passed onto the OAP toward the dewar window. The OAP is translated into place so that the HeNe spot focuses down to the

front of the diode. At this point, an IR detector is placed near the OAP along the path of the HeNe. The diode laser is turned on, and with a little luck, the detector indicates the presence of IR light. The position of the translation stage is optimized to focus the IR light directly onto the detector element. Beam collimation continues by repositioning the detector a few inches farther away from the OAP along the desired propagation path. Once again the position of the OAP is optimized to refocus the light onto the detector. This scheme is iterated through a series of distances where the goal is to focus the light onto a detector that is an infinite distance away. At each step, the beam diameter is measured for several points along the propagation path to help determine the position of the waist. Once the detector reaches the end of the table, the output of the laser is considered to be well-collimated with typical beam diameters of 1.0 – 1.2 cm.

To help manage the laser beam throughout the spectrometer, the light is passed through a series of optics that reduce the beam diameter by a factor of 4. The reducing telescope shown in Figure 2.10 is built from two BaF_2 lenses with the first lens (d = 50.8 cm, f = 20 cm) fixed so that the center is 4" above the table. The second lens (d = 25.4 cm, f = 5 cm) is mounted to an $x\,y\,z$ stage that is positioned $\approx$ 25 cm away. The stage is used to fine tune the position of the second lens so that the output is once again well-collimated. The reducing telescope also includes a pinhole spatial filter positioned at the beam waste. The pinhole is an adjustable iris that is also mounted to an $x\,y\,z$ stage, which enables the aperture to be precisely positioned to spatially filter the beam. The pinhole reshapes the transverse mode structure of the diode, which nominally involves oblique beam profiles as illustrated in Figure 2.2.

The aperture provides a profile that resembles TEM_{00} to help minimize noise due to clipping on other optics in the laser path. While spatially filtering remains feasible, the challenges of working with a pinhole include further reduction of the low power output and optical feedback to the laser cavity. A balance between these issues must be reached before the final alignment during an experiment.

After the telescope, the IR light is overlapped with a HeNe tracer beam to help pass the invisible beam through the remaining parts of the spectrometer. The overlap involves passing the red and IR light through a pellicle beam splitter (Edmund NT39-478) that transmits/reflects 80/20 at $\lambda = 4.2$ μm and 92/8 at $\lambda = 633$ nm. These two fractions of the infrared are used to detect the scattered CO_2 flux and determine the frequency throughout the scan. After the initial alignment with the overlapped beams, AR-coated germanium windows are used attenuate the HeNe light along both branches in the spectrometer.

The scheme to detect scattered CO_2 involves passing the first fraction of the beam (80%) through a soft focusing lens (f = 50 cm), after which the light is split again with a CaF_2 beamsplitter (50/50). As illustrated in Figure 2.11, the first half is passed through CaF_2 windows on the vacuum chamber into a modified Herriot cell.[8] The multipass is created with two spherical gold-coated mirrors (2" diameter, R = 20.0 cm) that are glued to JILA mirror mounts with epoxy at a distance slightly less than 40 cm apart. The soft focusing lens (i) reduces the beam diameter to prevent unintentional clipping on the first mirror in the chamber, and (ii) places the focus of the first pass near the center of the cell. The initial setup requires the first pass to land in the upper right corner of the far mirror. The mirrors are adjusted so that the beam

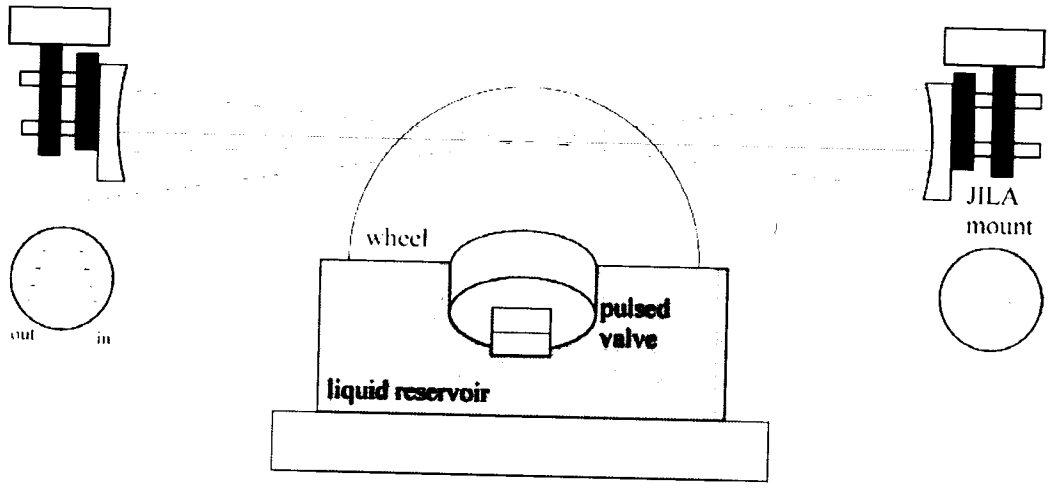

Figure 2.11 Modified Herriot cell configuration is used to pass the laser light multiple times (≈ 14 passes) over the liquid surface.

is reflected back to a spot that lands on the close mirror just above and to the left of the incoming beam. Next, this mirror is adjusted to pass the third spot back to the far mirror so that it falls just below and to the left of the previous spot. At this point, only the far mirror is adjusted to walk the remaining spots onto the opposite mirror in a parabolic pattern where the spot size grows and then shrinks with the total number of passes. The last pass refocuses the light under the close mirror to help minimize clipping as the beam leaves the chamber. The number of passes depends on the radial separation of the two spherical mirrors. More spots may be fit on the mirrors as the separation approaches 40 cm. After the beam leaves the chamber, another soft focusing lens (f = 20 cm) is used to help collimate the light. At the end, the beam is

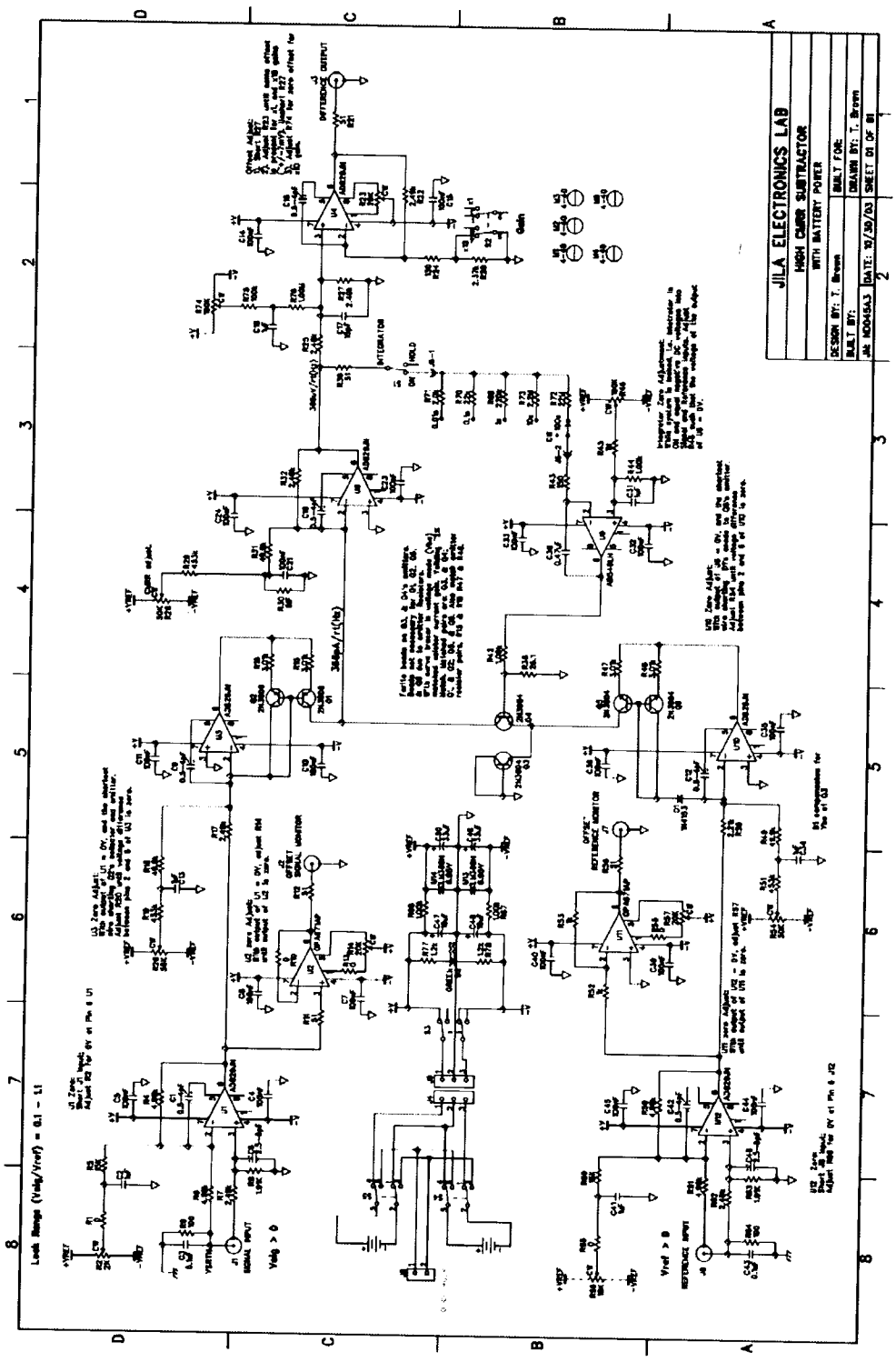

Figure 2.12 Noise subtraction circuit.

directed onto an InSb detector through a fast focusing lens (d = 12.7 cm, f = 2.54 cm) that maximizes the intensity of the signal.

The second half of the laser beam is passed directly onto a matched InSb detector that is used as a reference signal in a noise subtraction scheme. Voltages from the signal and reference InSb detectors are sent directly into servo loop subtraction electronics, which are illustrated in Figure 2.12 for the version used in these experiments. The circuit scales the voltage on the reference detector to match the value on the signal InSb, at which point the two voltages are subtracted to eliminate common mode noise. The scaling factor is determined by an integrator with a time constant that is appropriate for the duration of the scattering signal. The subtraction circuit also requires that the DC offset be set to zero, which is accomplished with a voltage summing junction controlled by trim potentiometers on the front face of the panel. The final setup requires fine adjustment of the common mode rejection ration (CMRR) knob to effectively subtract noise on the laser light. The detection scheme routinely yield absorption sensitivities of $\approx 2 \times 10^{-6}$ $Hz^{-1/2}$ for 0.3 μW of laser power.

2.2.5 Frequency Diagnostics

As the laser is tuned across an absorption profile, diagnostic components in the spectrometer are used to determine the frequency at each point in the scan. A reference gas cell provides absolute frequencies, while transmission fringes from a confocal Fabry-Perot cavity are used to determine the relative values at each data point. As depicted in Figure 2.1, the lock-in detection scheme involves chopping the IR + HeNe beams before the light is sent to either diagnostic element. A germanium

window reflects nearly all of the HeNe light onto a silicon photodiode, where the signal is used as a reference for the lock-in amplifiers. The chopped IR light is divided by a 50/50 CaF_2 beam splitter into two parts that are sent to the gas cell and etalon. Transmitted laser power in each diagnostic component is monitored with an MCT detector as a function of frequency throughout the scan. Voltages from the detectors are sent to lock-in amplifiers (Stanford Research Systems, SR510) that rectify these signals by heterodyning them against the frequency reference from the simultaneously chopped HeNe beam. The outputs are filtered to remove the 2f component, which results in a DC output that is recorded throughout the scan. At the end of the scan, the laser is blocked and the data acquisition software records an additional 50 points to measure any detector offset voltages.

The reference gas cell consists of three glass cylinders connected to a 250 mL glass bulb. Each tube is sealed on either side with sapphire windows and black wax, which allow the entire system to be evacuated and filled to a known pressure. The cylinders vary in length (1.99 cm, 5.82 cm, and 17.7 cm) so that absorption intensities may be easily adjusted throughout the experiment. In general, pressure in the cell is limited to $\approx$ 100 mTorr of CO_2 so that pressure broadening is a negligible contribution to line shape profile. The shortest cell is used for most of the ground state (00^00) transitions, while the longest path length is employed for vibrational hotband profiles. The triple cell is mounted by resting the bulb on top of a fixed ring stand. The bulb acts as a pivot in the ring so each of the three cells may be rotated into the path of the laser beam in front of an MCT detector. Two wires connected to the longest cell are used to switch the cells in a way similar to that of a puppeteer. These wires are

passed through a hole in the side of the purge box, where then the three cells may be interchanged under purge conditions. Recorded CO_2 absorption profiles are fit to a Voigt line shape that fixes the Gaussian component to a room temperature Doppler width. In this scheme, the extracted parameters include the Lorentzian component and the centerline transition frequency, which is used to define the absolute frequency in each scan. Internal state populations are calculated from the area under the curves with an analysis routine that includes normalizing magnitude of the absorbance to the length of the particular gas cell in place during the scan. A standard Boltzmann analysis ensures that the populations in the 00^00 and 01^10 vibrational states are well-fit by room temperature rotational and vibrational distributions.

Transmission fringes from an etalon are recorded during the scan to determine the frequency of each data point in the absorption profile. The etalon is constructed from a 27.5 cm long quartz tube (∅ 2.54 cm) with a 2.54 cm long piezo tube glued to one end. The cavity design involves two CaF_2 plano-convex mirrors that each have a 30 cm radius of curvature. One mirror is fixed directly to the PZT tube with nitrocellulose adhesive, while the other mirror is carefully positioned on the opposite end with a mirror mount attached to an *x y z* translation stage. A HeNe beam is used to set the second mirror at the confocal distance in the following way. The tube is placed in the beam path so that the cavity axis is parallel to the HeNe beam, but slightly off center (displaced radially by ≈ 0.5 cm) to help generate a bow-tie configuration within the cavity. The second mirror is coarsely aligned into the flared end of the quartz tube. The PZT is scanned with a high voltage saw toothed wave to allow multiple modes of the HeNe to transmit through the cavity. Light is monitored

on a Si photodiode as the second mirror is accurately positioned with the translation stage. Fringes sharpen as the cavity length reaches the confocal distance, which ultimately leads to a measured finesse of 18 for the HeNe beam. The mirrors used for the current cavity are 91% and 96% reflective at 632.8 nm, which corresponds to a theoretical finesse of 23. At $\lambda = 4.2$ μm, the finesse is a different story based on reflectivity values of 65% and 46% to yield a theoretical finesse of 2.6 for the bowtie configuration. Unfortunately, the actual transmission fringes appear to yield a finesse of 0.1 – 0.5. Such a discrepancy has not been fully resolved, but may be due to the line width of the laser, angle dependence of the coating, or perhaps something else. In any event, these fringes still provide adequate signals to linearize the frequency axis in the scans. The free spectral range (FSR) of the cavity is measured by counting the number of fringes between two closely spaced CO_2 transitions. Values are measured at a series of frequencies in the CO_2 spectrum, where the average is 250.52 MHz and standard deviation of five measurements is 1.12 MHz. Frequency interpolation between the transmission fringes is covered in the data analysis discussion in Section 2.6.

2.3 Molecular Beam

2.3.1 Overview

The incident gas molecules are prepared in a molecular beam where the supersonic expansion provides a narrow distribution of velocities around an average that is controlled by the components in the gas mixture. The molecular jet supersonically cools CO_2 into the lowest few rotational states. Extensive details of

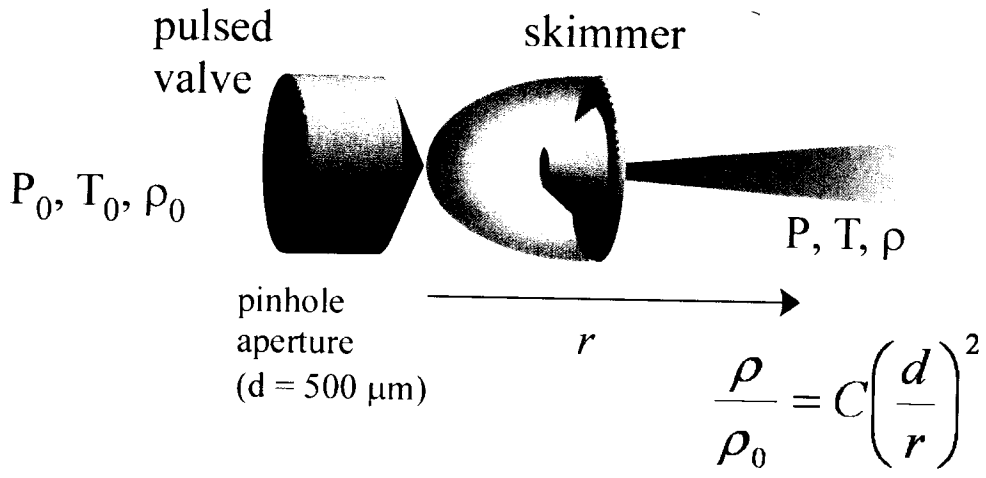

Figure 2.13 Incident CO_2 molecules are prepared in a pinhole supersonic expansion that is skimmed to generate a molecular beam.

the theory behind molecular beams have been presented elsewhere.[1,9] The primary focus of the current section is to provide a brief overview of the general operating principles that determine the optimal conditions for the scattering experiments. These ideas are followed by a description of the specific pulsed valve configurations and methods that are employed to characterize the incident beam.

The molecular beam is generated with pinhole aperture in a pulsed valve that is illustrated in Figure 2.13. In general, a supersonic jet requires the flow of gas from a high (P_0) to low (P_∞) pressure region, which generates an expansion that adiabatically cools the atoms and molecules. Supersonic flow is reached when (i) the mean free path of the gas in the nozzle is much less than the pinhole diameter (d), and

(ii) the pressure difference between the two regions is larger than a factor of two. These two requirements ensure that collisions with the walls of the pinhole and background gas in the chamber are negligible. Under these circumstances, the pressure, temperature, and number density of molecules in the expansion are determined by the type of gas in the mixture and the initial conditions in the stagnation region. For example, the number density for a monatomic gas along the expansion axis (r) is,

$$\frac{\rho}{\rho_0} = C \cdot \left(\frac{d}{r}\right)^2, \qquad (2.1)$$

where ρ_0 is the number density in the stagnation region and $C \approx 0.143$. The expression for an expansion of a polyatomic gas follows the same form, but the value of C changes slightly based on the different heat capacities of the particular gas. The terminal velocity of the gas in the jet is defined by the temperature in the valve and components of the mixture. Depending on the desired incident energy, CO_2 is mixed with hydrogen, helium, neon, or argon before being passed through a room temperature valve. The terminal velocity for molecules in a jet is,

$$v_{term} = \sqrt{\frac{\gamma}{\gamma - 1}\frac{2kT}{w}}, \qquad (2.2)$$

where w is the average molecular weight of the mixture, γ is the ratio of the heat capacities (C_p/C_v), and T is the temperature in the stagnation region. Velocities of the gases in the molecular beam are characterized for the various mixtures in the following section.

With these relationships in mind, the scattering experiments are designed to ensure that the measured CO_2 distributions exclusively reflect nascent interactions

with the liquid. Simple back-of-the-envelope calculations help illustrate the important criteria for the initial operating conditions. First, the number density at the surface and terminal velocity are combined to determine the incident flux of CO_2 per unit area, which we limit to ≈ 0.1 monolayer (ML) per gas pulse to help guarantee the single interaction conditions. Fractional surface coverage is calculated from the flux and length of the typical gas pulse, which are combined and compared to the typical number of exposed surface sites ($\approx 4\times10^{15}$ sites/cm^2). Typical operating conditions involve CO_2 in a hydrogen carrier gas (P_0 = 100 Torr) where the pinhole (∅ 400 μm) is positioned 11 cm from the surface. The total number density at the surface ($\approx 8 \times 10^{12}$ #/cm^3) and the terminal velocity (1.42×10^5 cm/s) result in a flux of $\approx 1 \times 10^{18}$ #/cm^2/s. Typical 300 μs gas pulses lead to a deposition of $\approx 3 \times 10^{14}$ molecules/cm^2. This value reflects the total flux of $CO_2 + H_2$, which is kept below 0.1 ML in the experiment.

Another important aspect of the molecular beam involves the position of the Mach disk with respect to the pinhole-to-surface distance. The disk is a shock wave created in the region where the densities of the gas in the expansion and background approach similar values. As the jet begins to equilibrate with the background gas, the bulk velocity drops below the local speed of sound, at which point the molecular beam begins to break down. An empirical relationship for the distance of the Mach disk of a pinhole expansion is given by

$$r = 0.67 \cdot d \cdot \left(\frac{P_0}{P_\infty} \right)^{1/2}. \qquad (2.3)$$

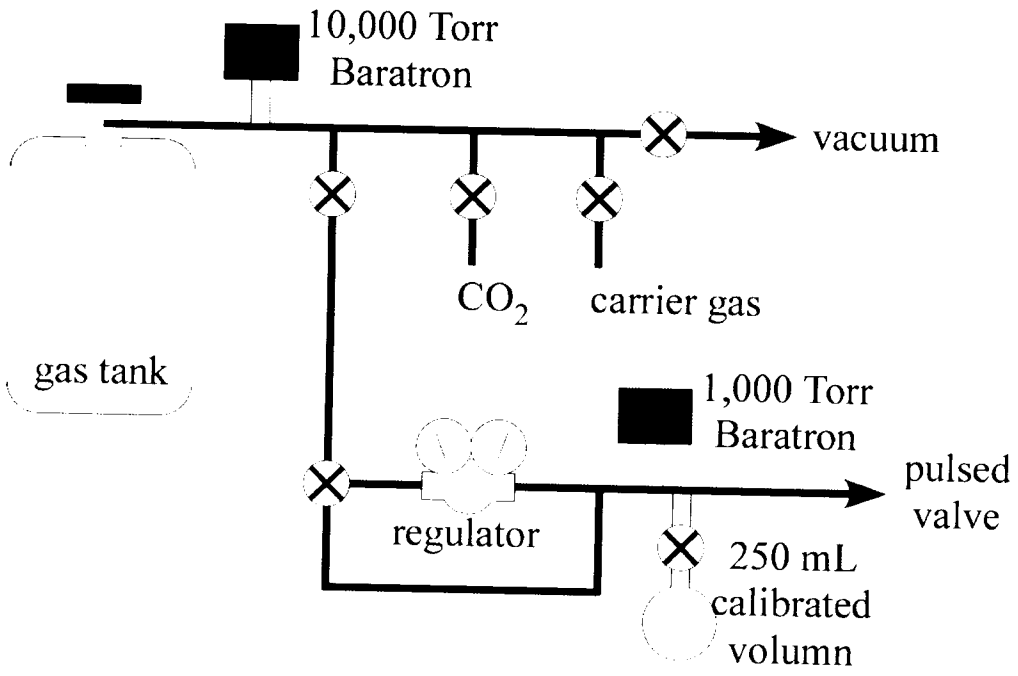

Figure 2.14 Schematic of the gas manifold that is used to mix and deliver CO_2 to the pulsed valve.

Typical experiments involve stagnation and background pressures of P_0 = 100 Torr and P_∞ = 1–3 × 10^{-5} Torr, respectively, with a 400 μm pinhole aperture, which estimate the Mach disk to be ≈ 50–100 cm from the pinhole. Importantly, this value is an order of magnitude larger than the distance from the pinhole to surface to make certain that the molecular beam remains stable for the scattering experiment.

2.3.2 Gas Manifold

The gas for the molecular beam is delivered to the pulsed valve through a manifold that is illustrated in Figure 2.14. The plumbing of the system is configured to mix two or more gases, and then deliver the mixture to the pulsed valve in a

controlled fashion. The manifold is constructed from copper, brass, and polyflo tubing, which are isolated at various sections with stainless steel ball valves. The lines may be evacuated with a small mechanical pump that is connected through another isolating ball valve. Gas mixtures are made and stored in a standard 5 gallon propane tank, which is connected to the manifold with an internal safety valve. These valves are included in most propane tanks to limit the flow through the valve. Importantly, the input pressure must reach a certain threshold before the valve opens and releases a small squeal. Mixtures are made by filling the tank with CO_2 and a seeding gas, where the partial pressure of each component is measured with a 10,000 Torr capacitance manometer pressure gauge (MKS Baratron 722A) at the inlet of the mixing tank. The general procedure involves first filling an evacuated tank with 100–200 Torr of CO_2 from a standard 1A tank that is connected to the manifold. Next, the buffer gas is added to the propane tank in spurts to turbulently mix the contents of the tank. This process is continued until the pressure in the tank corresponds to a mixture of 10% CO_2, i.e. a total pressure of 1000–2000 Torr. The final step is the easiest since it only involves waiting overnight for the gases to thoroughly mix.

After a mixture has been made, the gas is passed to the pulsed valve through the remaining portion of the manifold. To precisely control the pressure in the valve, the CO_2 mixture flows through a single stage stainless steel regulator (Matheson Tri-Gas, Inc, model 3494) that drops the pressure from above atmosphere to $\approx$ 100 Torr. The pressure is monitored by a second manometer (MKS Baratron 722A), which is rated to measure values between 0–1000 Torr. The output of both pressure gauges is displayed by a digital voltmeter where the voltage is directly proportional to the

pressure on a 0–10V scale. An additional feature of this section of the manifold is a calibrated glass bulb with an isolating valve. The bulb is attached to the system with a standard 10 mm glass o-ring seal and metal clamp. The known volume (262.8 mL) of this bulb plus the gas manifold (109.6 mL) enables us to determine the absolute flux through the pinhole on the pulsed valve. Polyflo tubing is used to connect the output of the regulator with the valve through an Ultra-torr feedthrough on the side of the main vacuum chamber.

2.3.3 Pulsed Valve and Skimmer

The gas-liquid scattering studies revolve around a molecular beam that is generated with a piezo-controlled pulsed valve. Two versions of this PZT valve have been used, both of which have been built in the JILA machine shop. The older of the two valves is used in the gas-liquid scattering chamber, while the newer valve resides in the gas + SAMs experiment. General features of both valves are based on the designs by Proch and Trickl,[10] where small modifications have been included to streamline the initial setup and improve overall performance. The setup procedure has been outlined in detail within previous experimental reports; therefore, a basic description of the valves is included to provide details about usage and performance characteristics. Schematics are illustrated in Figure 2.15 to help describe the essential features of both valves. In addition, the high voltage drivers for both valves are illustrated in Figures 2.16 and 2.17.

In general, the valve is constructed in two parts to provide access to the interior components that are normally sealed from the vacuum chamber with a series of o-rings. The front part of the valve houses the piezo disk (Physik Instruments, P-

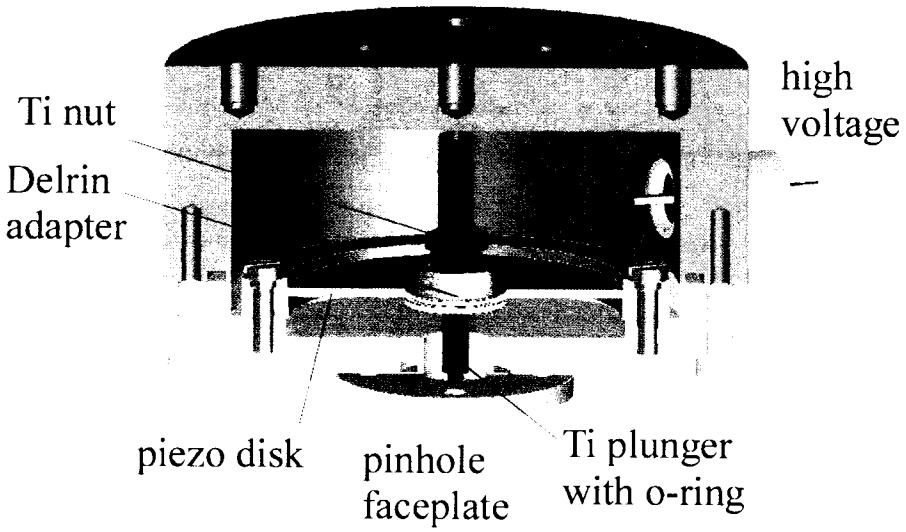

Figure 2.15 Cross-sectional schematic of piezoelectric-controlled pulsed based on the initial designs of Proch and Trickl.

286.23) that opens and closes the valve. The PZT elements are designed to buckle at the center when a high voltage is applied to the crystal, which then provides a way to translate a plunger away from the pinhole aperture to create a pulse of gas. As shown in the schematic, two Delrin adapters are mounted to the center of the hole in the middle of the circular PZT disk. These two pieces are threaded together and tightened to the disk with a home-built brass spanner. The inside Delrin adapter is also threaded so that the titanium plunger may be mounted to center of the PZT. Once these three parts are attached to the disk, the PZT is bolted securely to the front frame of the valve. The pinhole aperture face plate is mounted to the front face of the valve with four screws that compress an o-ring seal. The general sealing mechanism involves translating the plunger away from the pinhole to allow gas flow out of the valve. To create a vacuum seal, a small o-ring is attached to the tip of the plunger so

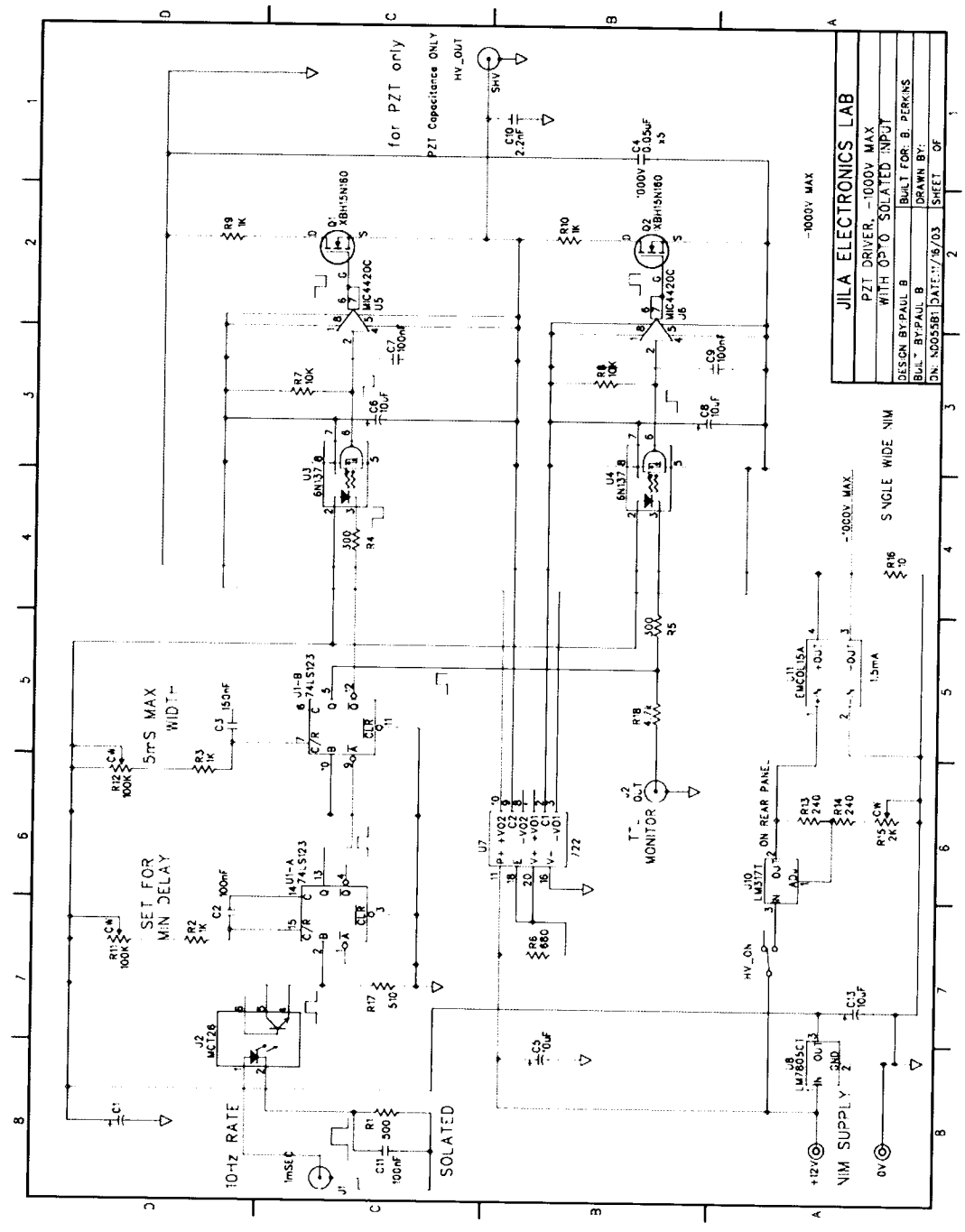

Figure 2.16 Pulsed high voltage driver for the PZT valve used in the gas–liquid scattering chamber.

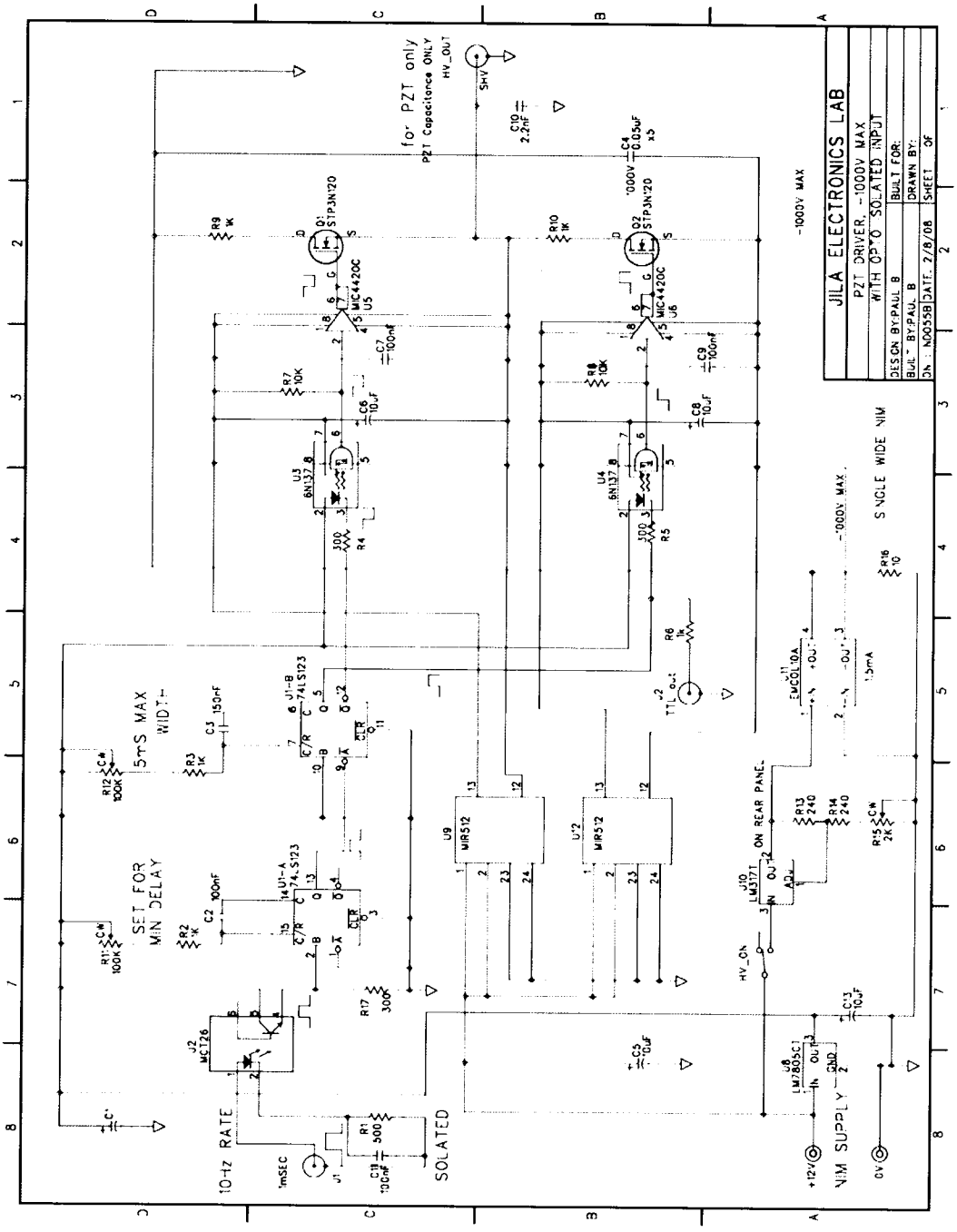

Figure 2.17 Pulsed high voltage driver for the PZT valve used in the gas–SAMs scattering chamber.

that the o-ring sits flush on the aperture face plate when the PZT element is relaxed to its neutral position. The plunger is positioned in the Delrin adapters so that a slight resistance is felt to indicate that the o-ring has made contact with the face plate. The plunger is then carefully locked into position by a titanium nut.

At this point, the valve is tested to ensure the plunger appropriately seals the valve. The procedure requires an adapter flange (Figure 2.18) that is mounted directly to the side of the gas-liquid vacuum chamber. The front part of the valve is fixed to the flange where an o-ring seals the face to the chamber so that the pinhole is directed through an opening into vacuum. Before the chamber is evacuated, a microphone is mounted on a rod and passed through an Ultra-torr fitting on the adapter flange. The microphone is positioned in front of the pinhole where the rod may then be moved to translate the microphone along the molecular beam expansion axis. Once setup, the chamber is evacuated to provide an initial test of the plunger seal. If the valve leaks, then the titanium bolt is loosened so that the plunger may be adjusted to create a proper seal. To characterize the gas pulse, the PZT element is connected to a high voltage driver that provides control of the duration and delay of the gas pulse. The initial setup involves an external TTL trigger that is supplied either from a function generator or from a computer-controlled digital-to-analog output. With the initial voltage to the PZT set low, a trim potentiometer on the valve driver is slowly adjusted to increase the magnitude of the pulsed voltage to the point where the valve opens and gas flows through the pinhole. The PZT element typically translates $\approx$ 100 μm at the maximum voltage ($V_{max} = -1000V$), which then requires the driver to output something comparable to adequately open the valve. Typical

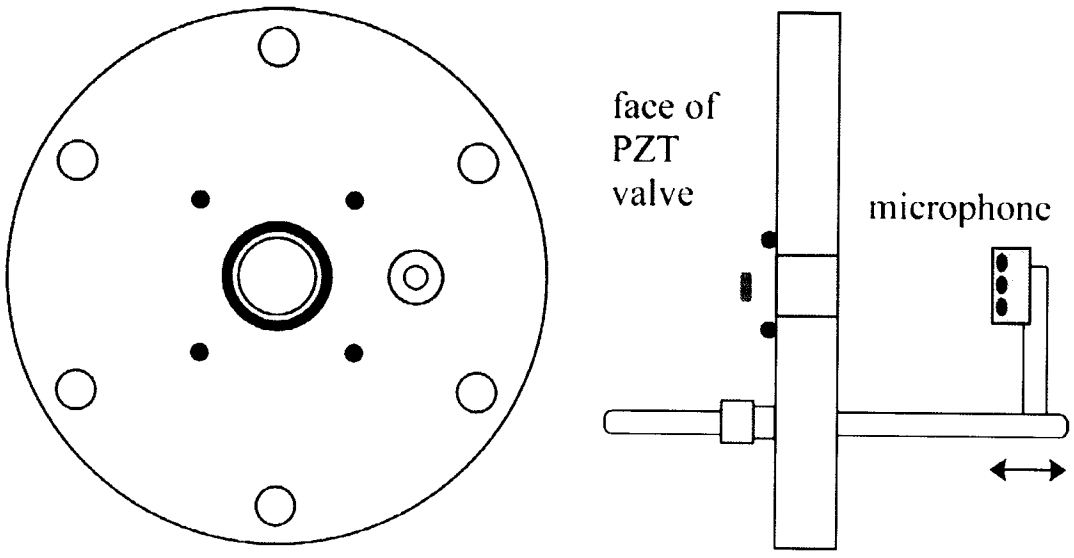

Figure 2.18 A custom-built flange is used to mount the PZT valve to the gas–liquid chamber for initial setup and characterization. A microphone is used to monitor the gas pulse as the valve and driver are optimized.

voltages that are required to open the valve range from –300 to –400 V in both of the initial setups. Once the valve is pulsing, the microphone signals are monitored through a home built amplifier illustrated in Figure 2.19. The opening voltage, pulsed width, and delay are set to optimize the time profile of the gas pulse. In general, the driver voltage is set just above the point where the amplitude of the microphone signal remains constant. Additionally, the width is set to $\approx 300 - 350$ μs to ensure the valve fully opens with every pulse.

Once the initial valve setup is complete, the front face is removed from the test flange and reassembled with the other half of the valve. The remaining steps include connections to the gas manifold and high voltage power supply. On the liquid chamber valve, a gas line from the manifold is attached through an Ultra-torr

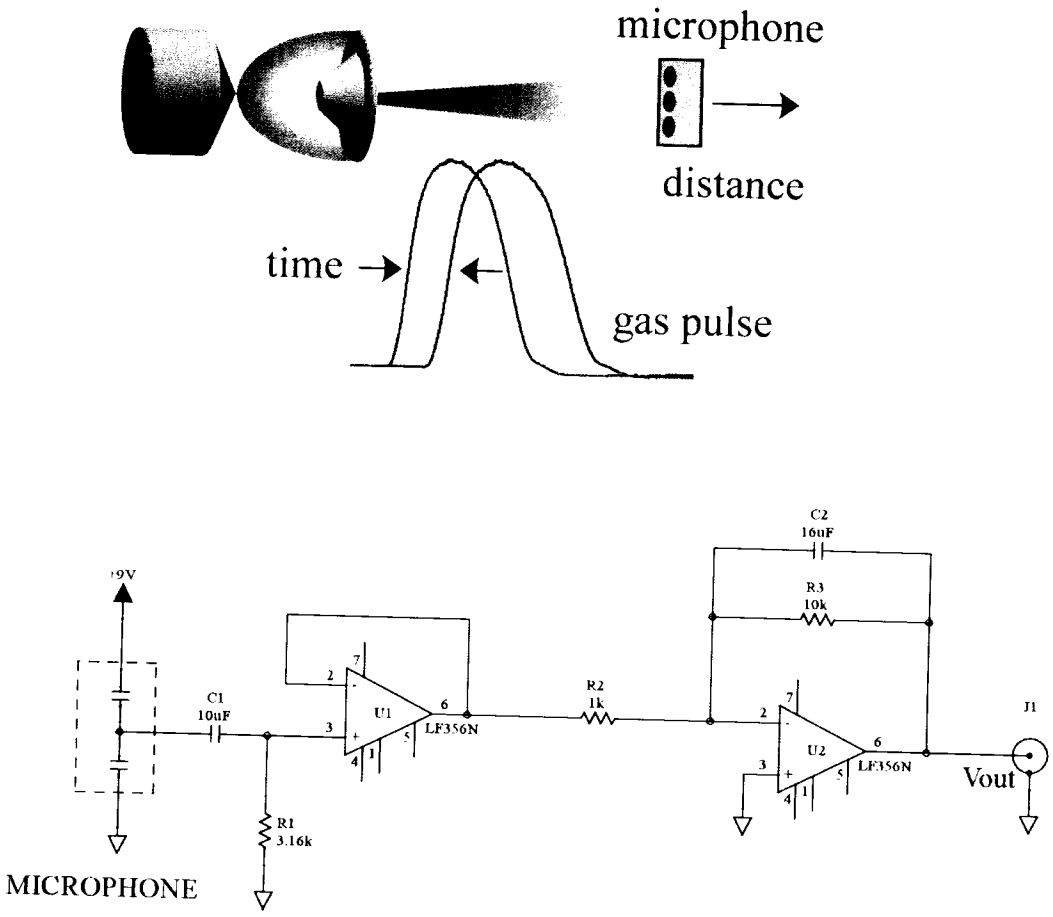

Figure 2.19 Schematic of the time-of-flight experiments used to measure the centerline velocity of the gas pulse. The microphone signal is processed by the given amplifier circuit.

connection on the back side of the valve body. This feedthrough limits the total pressure that can be passed into the valve since the sealing connection is simply a friction fit. Negative voltage is supplied to the PZT disc through a MHV connector, where the body of the valve provides the reference to ground. The newer valve design incorporates a VCR connector to deliver the gas, and a single isolated pin to

transfer the high voltage. Once again, the body of the valve is grounded to provide the potential difference for the PZT. Both valves are mounted through tapped-holes on the backside. Experiments have been set up in various configurations where the valve bodies are positioned in front of a skimmer in a specific scattering configuration.

The jet expansion is skimmed to reduce the angular divergence of the beam so that out-of-plane scattering may be detected. The skimmers (Beam Dynamics, Inc.) are constructed from nickel with an ultra-thin aperture edge that is designed to reduce interference effects in the molecular beam. Skimmers in the initial normal incidence studies are 5.0 mm in diameter and mounted on a plate positioned 2.5 cm downstream along the expansion axis. As space became cramped in glancing incident experiments, a smaller 3.0 mm diameter version is used in a similar configuration with the skimmer orifice 1.5 cm away from the pinhole. In both cases, the skimmer is first placed between aluminum and Teflon adapters to provide additional structural support. These pieces are then mounted to a plate that is bolted to the scaffolding that supports and positions the pulsed valve with respect to the liquid surface. A laser pointer is used to align the center of the aperture with the pinhole along the expansion axis before the final bolts are tightened to fix the skimmer in place. To do this, the laser is mounted in a machined adapter that fixes the output in the same position as the pinhole, where then this adapter may be attached in place of the pulsed valve. Geometrically, the skimmer configuration restricts the angular divergence of the molecular beam to $\pm 6^{\circ}$.

2.3.4 Incident Beam Characterization

Properties of the supersonic jet are characterized to determine the incident translational, angular, and internal state distributions. The PZT valve is a remarkably stable source that showed no significant deviations after the initial setup. Translational and angular distributions are analyzed with a several analytical tools that include (i) a simple microphone time-of-flight analysis, and (ii) high resolution Dopplerimetry analysis of the absorption profiles. In terms of the internal states, populations are recorded for a series of rotational states in both the ground (00^00) and bend excited (01^10) vibrational manifolds. Brief details of these results have been presented throughout each chapter. Therefore, we cover the basis of the techniques and measurements in more detail to list the methods that lead to a systematic characterization of the incident CO_2.

2.3.5 Translational Distributions

Velocities of CO_2 in the pinhole expansion span three directions ($x\ y\ z$) where x and y are the same based on the azimuthal symmetry of the aperture. Two independent techniques are used to characterize the distributions both (i) along, and (ii) perpendicular to the expansion axis. To help illustrate these techniques, a sample transient absorption profile is plotted in Figure 2.20 for R(0) at the centerline transition frequency (ν_0) to show the general temporal profile of the pulse. These pulses are also monitored with the microphone where the transient signals are nearly the same. In a simple time-of-flight experiment, the microphone is attached to a rod so that the position of the sensor is adjustable through an Ultra-torr feed through on the opposite side of the vacuum chamber. As illustrated in Figure 2.19, time signals

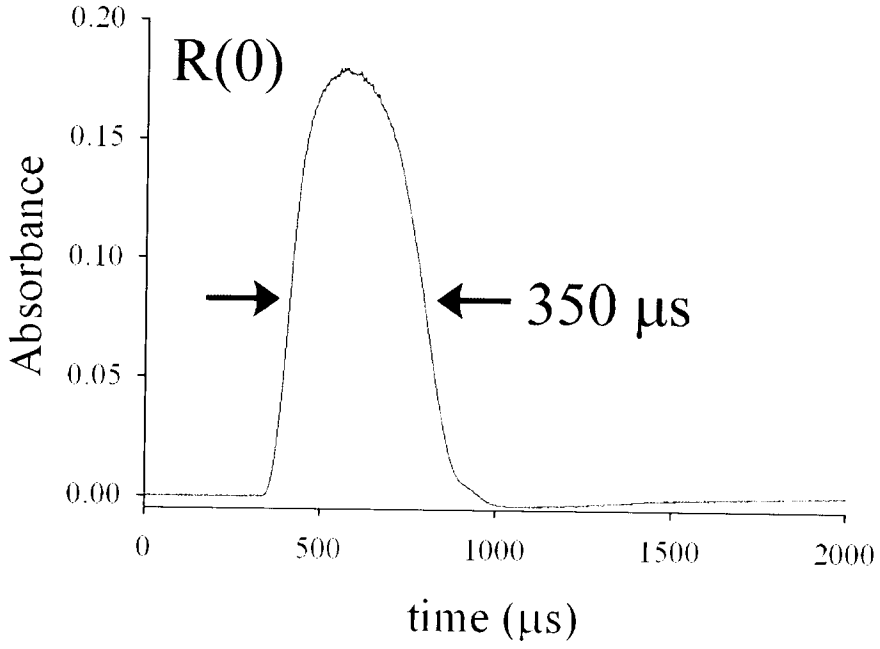

Figure 2.20 Centerline (v_0) absorption profile for J = 0 in the incident beam.

are recorded for a series of distances where the microphone is moved away from the pinhole along the expansion axis. The easiest times to measure are those along the front edge of the FWHM becausethe slope is the steepest. The best-fit line to a simple distance versus time analysis reflects the average velocity of the gas in the molecular beam. Sample plots are illustrated in Figure 2.21 for mixtures of CO_2 with argon, neon-70, helium, and hydrogen. Values reported in Chapter 4 show excellent agreement between these measured values and those that are calculated from the relationship in equation 2.2. For example, the measured velocity for the hydrogen expansion is $1.41(9) \times 10^5$ cm/s, whereas the calculated number is 1.42×10^5 cm/s.

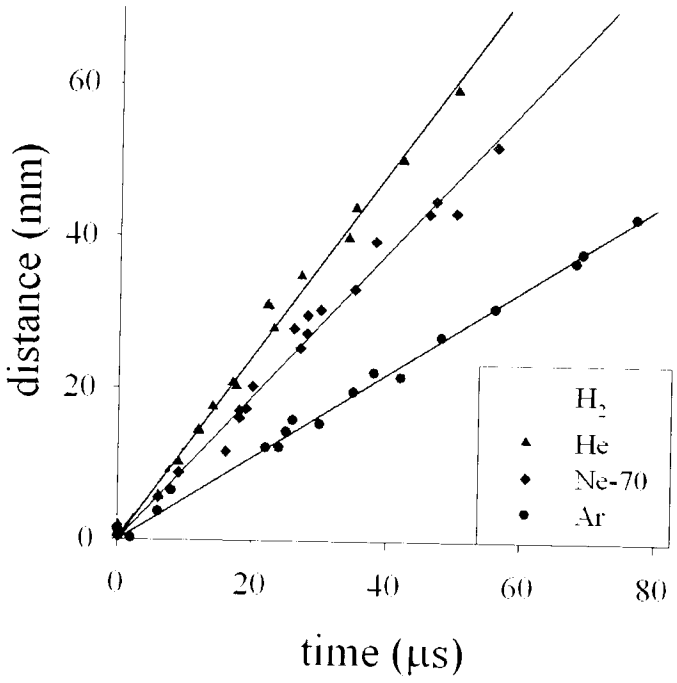

Figure 2.21 CO_2 velocities are measured with the microphone in a TOF experiment for gas mixtures that include H_2, He, Ne-70, and Ar.

Similar agreement is found between the other measured and calculated beam velocities.

To characterize velocities along the *x* and *y* direction, Doppler-broadened absorption profiles are recorded and analyzed for a series of experimental configurations. The frequency at which CO_2 absorbs depends on the projection of its velocity along the laser propagation direction. These detuning frequencies ($\nu-\nu_0$) reflect the Doppler shift associated with translation, where

$$\nu - \nu_0 = \nu_0 \cdot \frac{v}{c} \qquad (2.4)$$

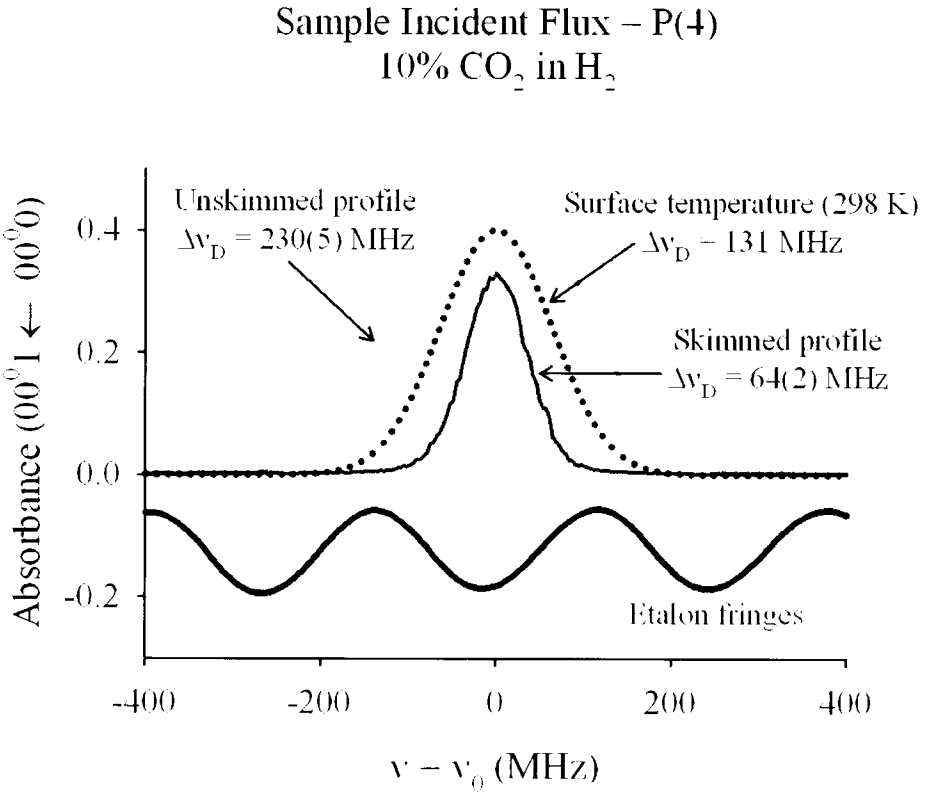

Figure 2.22 Sample incident beam absorption profile.

The simplest setup involves passing the laser through the molecular beam so that the expansion axis and laser propagation direction are orthogonal. Sample absorption profiles are illustrated in Figure 2.22 for an unskimmed and skimmed supersonic expansion for a laser scan of ≈ 1 GHz. The profiles are modeled with a Voigt line shape in *voigtb.x*, which is a convolution of Gaussian and Lorentzian functions. The Gaussian component characterizes the translational distribution and the small Lorentzian factor accounts for the residual line width of the Pb-salt diode laser ($\Delta\nu_{laser}$

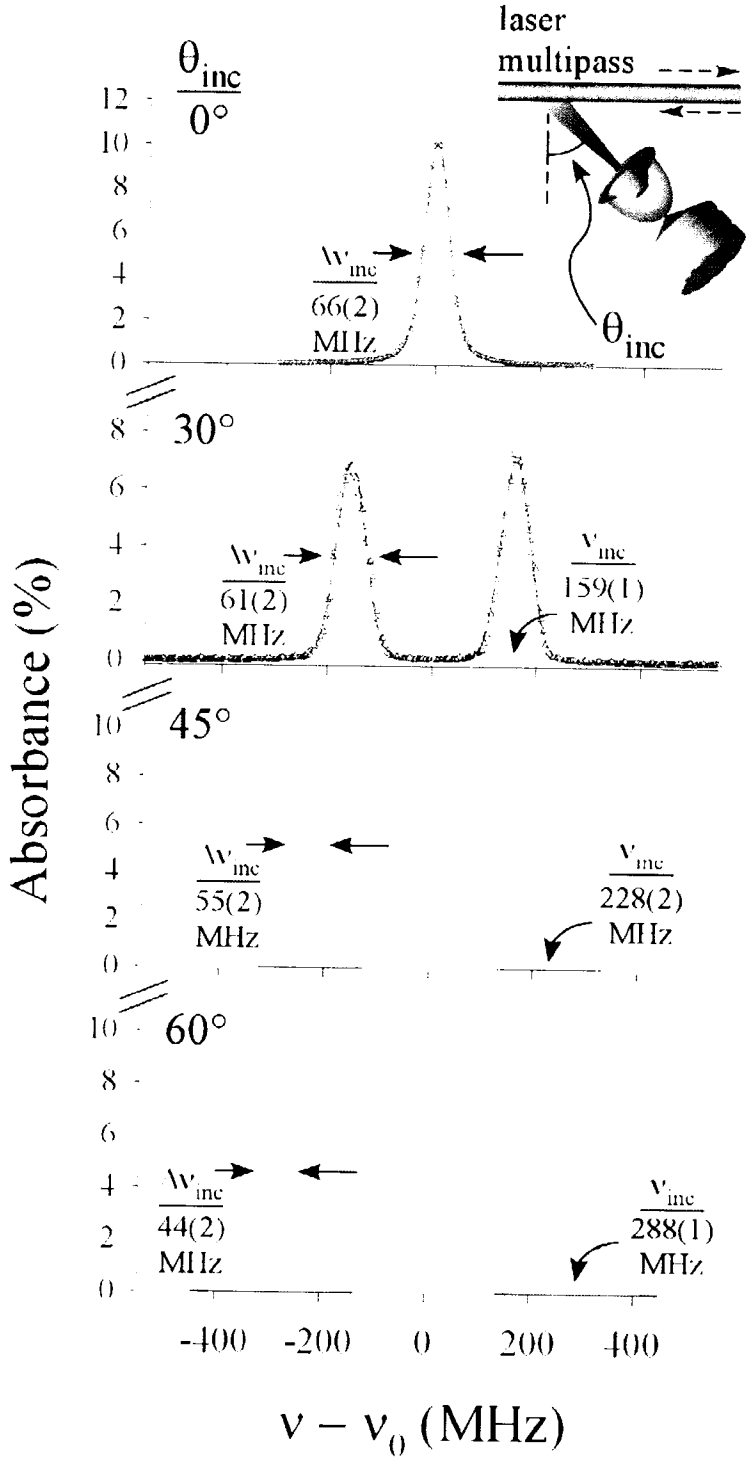

Figure 2.23 Incident beam absorption profiles measured in the $\varphi_{laser} = 0°$ configuration for $\theta_{inc} = 0°– 60°$. Line shape analysis is used to extract full width-half maximum (FWHM) and peak frequency shifts for each configuration.

$\approx$ 20 MHz). The extracted FWHM values show that the skimmer reduces the angular divergence from a half angle of $\approx$ 20.3° to 5.5°. Importantly, the Doppler broadening is smaller than a typical room temperature width of $\approx$ 129 MHz, which allow us to investigate energy transfer into translational distributions of scattered CO_2.

The Dopplerimetry analysis is also used to characterize the centerline velocity of the expansion in a series of experiments that complement the TOF studies. From the cartoon illustration in Figure 2.23, the molecular beam is moved into the $\varphi_{laser} = 0°$ configuration so that the expansion axis intersects the laser beam at a fixed incident angle (θ_{inc}). As θ_{inc} extends beyond 0°, the absorption profiles split into two peaks reflecting the back-and-forth nature of the laser multipass. In these configurations, the centerline absorption frequencies are proportional to the projection of the average molecular beam velocity, while the Gaussian FWHM reflects a convolution of the angular andvelocity spread in the beam. Profiles have been fit to a model that extracts the centerline frequency and FWHM for each J-state, which are plotted in Figure 2.24. Both values show a state dependence that most likely reflects velocity slip effects of CO_2 in the expansion. The centerline frequencies of each state are converted to velocity, at which point the fractional population per J-state is used to calculated a weighted average velocity. These values reflect the projection of the terminal CO_2 speed in the jet. The spread in velocities is obtained from a simple Gaussian deconvolution of the FWHM that accounts for the ± 5.5° spread in the molecular jet. Extracted values for $\Delta v/v_\infty$ are 0.105, 0.108, and 0.093 for $\theta_{inc} = 30°$, 45°, and 60°, respectively with an average of 0.102(8).

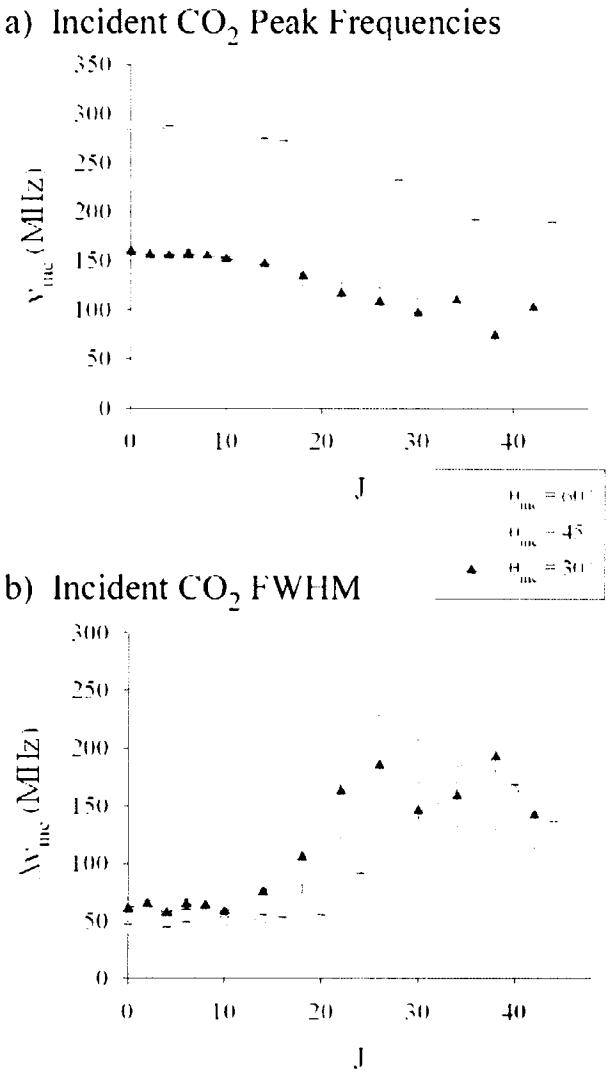

Figure 2.24 Dopplerimetry analysis of the incident beam line shapes extracts (a) peak frequencies and (b) FWHM as a function of J-state for each incident angle.

2.3.6 Internal State Populations

The internal state distribution depends on the collision conditions during the expansion. In general, higher pressures and larger pinhole apertures lead to colder distributions since the number of collisions scales linearly with both parameters. While many studies in the group have exploited these conditions to generate clusters, the scattering experiments require CO_2 monomer in the molecular beam so that the measured dynamics reflect the nascent interactions between individual molecules that collide with a liquid surface. To test the clustering conditions for a given mixture, J-state absorption profiles are recorded for a series of valve pressures to determine the regime where clustering is prevalent. The profiles are integrated over all Doppler detuning frequencies to generate a column integrated density ($A_{v,J}$). Typical clustering tests include populations in $J \approx 0 - 8$ since more than 90% of the total population is cooled into these states in the supersonic expansion. Column densities for each J-state are plotted versus stagnation pressure in Figure 2.25 for a series of mixtures that include CO_2 with (a) hydrogen, (b) helium, (c) neon-70, and (d) argon. In addition, the sum of each column density is plotted to show the regime where the signal growth is linear with pressure. In each case, the curves are linear until ≈ 150 Torr, at which point the monomer signal starts to decrease as clusters form in the jet. Optimal operating pressures are typically set at 100 Torr in the scattering experiments to ensure the dynamics only involve collisions between CO_2 monomer and the liquid surface.

The general characterization of the internal state distribution involves a standard Boltzmann analysis of the populations in the 00^00 and 01^10 vibrational

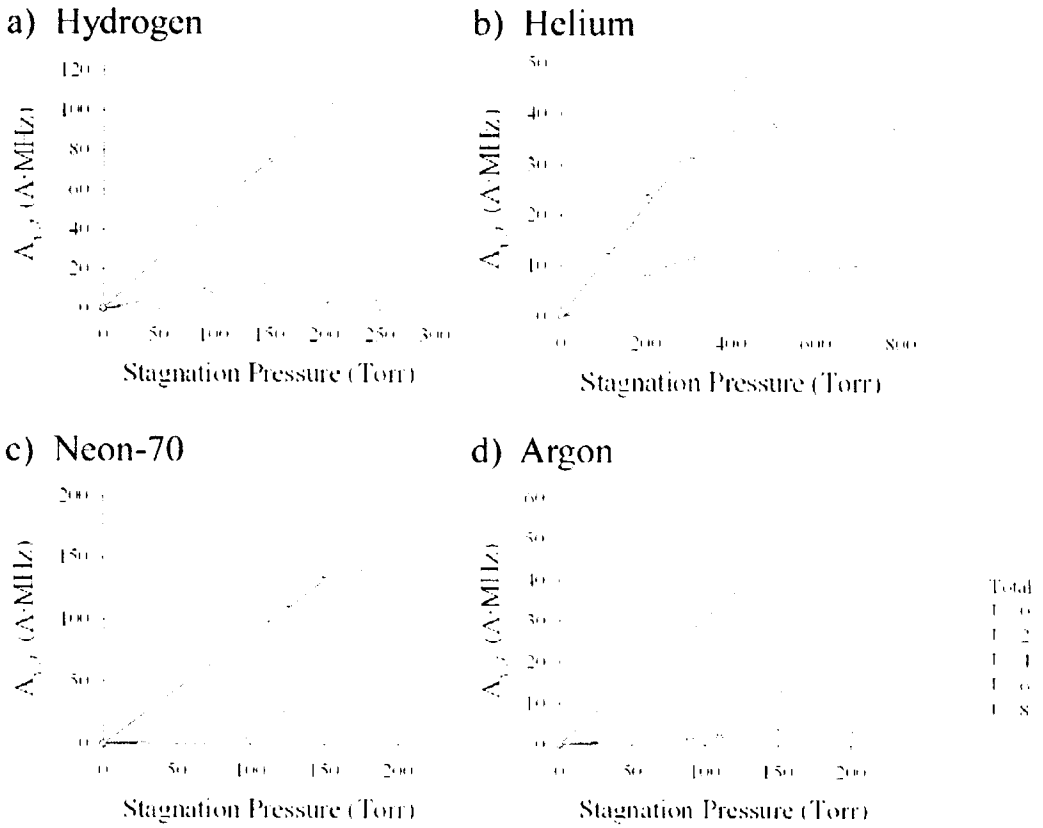

Figure 2.25 Growth curves of monomer CO_2 determine the effects of clustering in the molecular beam. Column integrated densities ($A_{v,J}$) are measured as a function of J-state and pressure in the stagnation volume of the pulsed valve.

manifolds. Absorption profiles are recorded for a series of J-states within each vibrational state. Details of these measurements are covered in Section 2.6, which explains the general detection scheme. To generate the population per quantum state, the absorption profiles are integrated to generate $A_{v,J}$. To properly account for the Hönl-London line strength factors (S_J), the column densities are divided by either J/(2J+1) for P-branch or (J+1)/(2J+1) for R-branch transitions. These values are now directly proportional to the product of the CO_2 number density and absorption path

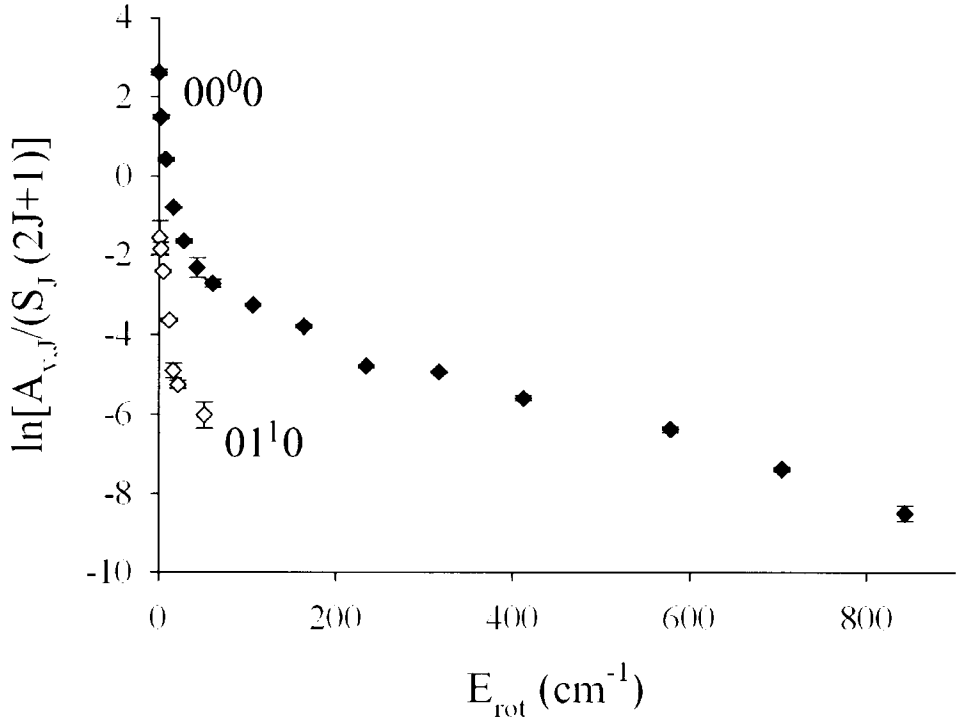

Figure 2.26 J-state distribution for CO_2 in the incident molecular beam. Populations are measured for ground (00^00) and bend-excited (01^10) vibrational states.

length. The column densities for rotational states in both vibrational manifolds are plotted against the rotational energy in a standard Boltzmann analysis. Sample distributions are plotted in Figure 2.26 for CO_2 in H_2 to illustrate the supersonic cooling in the expansion. The best fit line to the lowest rotational states show that the rotational temperature is $T_{rot} \approx 15 - 20$ K. The fractional difference between the two vibrational states provides an estimate to the vibrational temperature, $T_{vib} \approx 170$ K.

While the majority of the population cools into the lower rotational states, the Boltzmann plot also reveals a small fraction of the incident CO_2 remains in higher J

states. This nonthermal distribution reflects the inefficient cooling of CO_2 out of high rotational states in a pinhole expansion. In scattering experiments that involve passing the incident molecules through the laser beam, the initial rotational state populations are measured for a series of J-states so that these populations can then be subtracted from the values of the scattered CO_2. At normal incidence, a comparison of scattered to incident flux populations shows that the ratio is between 10 and 50 for rotational states greater than J = 10. In these experiments, values for the incident column densities are subtracted from the scattered flux before the populations are analyzed with the two-temperature Boltzmann model. In other scattering configurations with $\theta_{inc} > 0°$, the incident beam typically misses the laser and no subtraction is needed. These conditions were tested in every experiment so that the appropriate values could be subtracted if necessary.

2.4 Liquid Surface

2.4.1 Liquid Chamber

The bulk of experiments involve scattering CO_2 off liquid surfaces under high vacuum conditions. Surfaces are generated from methods first developed by Lednovich and Fenn, who used a glass wheel that slowly rotates ($\approx 0.5 - 1$ Hz) through a reservoir of liquid to prepare a liquid surface. A razor blade scrapes away the top liquid layer to reveal a renewed liquid surface for the scattering experiment. The pulsed valve and wheel assembly are housed within an 60 liter aluminum chamber that is constructed as a cube with interchangeable aluminum and plexiglass flanges. The chamber is evacuated with a 6" diffusion pump (VHS-6, 1000 l/s),

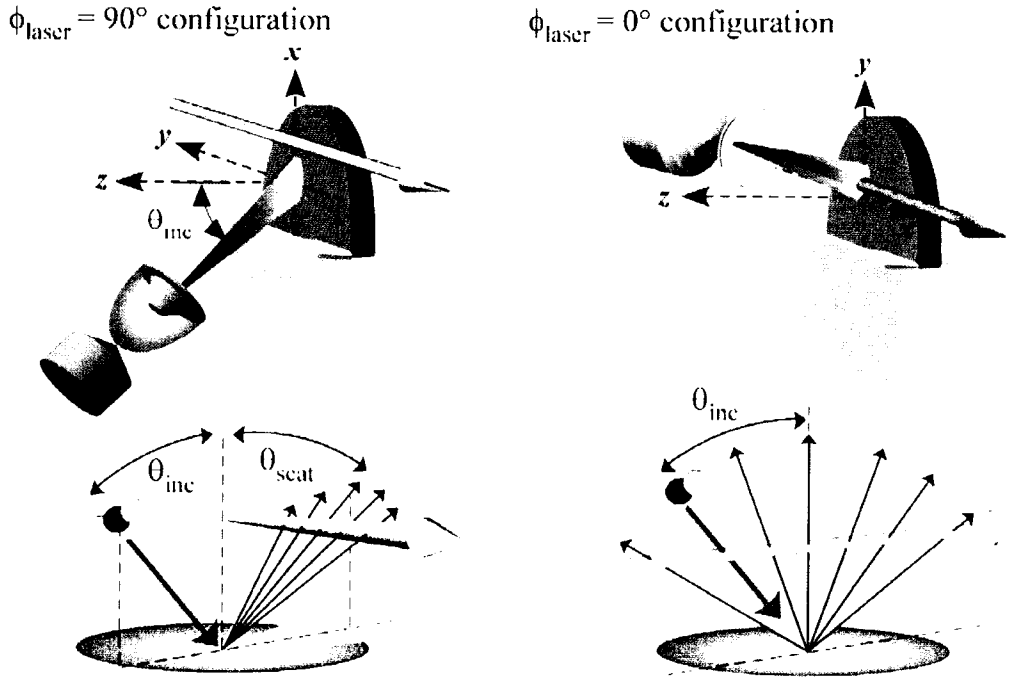

Figure 2.27 Experimental configurations to measure scattered CO_2 over the 2π hemispherical scattering volume.

which is separated from the cube with a gate valve and liquid N_2 cold trap. The pump is backed by an Edwards E2M30 rotary vane mechanical pump with plumbing that includes 3" rubber tubing and a 3" gate valve to isolate the diffusion pump if necessary. The tubing is attached to a block of concrete submerged in sand for additional vibrational isolation. Thermocouple pressure gauges are mounted directly to the chamber and inlet of the roughing pump to monitor the pressure while the chamber is roughed out from atmosphere. In addition, an ion gauge mounted to the top flange to monitor the system pressure when the diffusion pump is on. The base

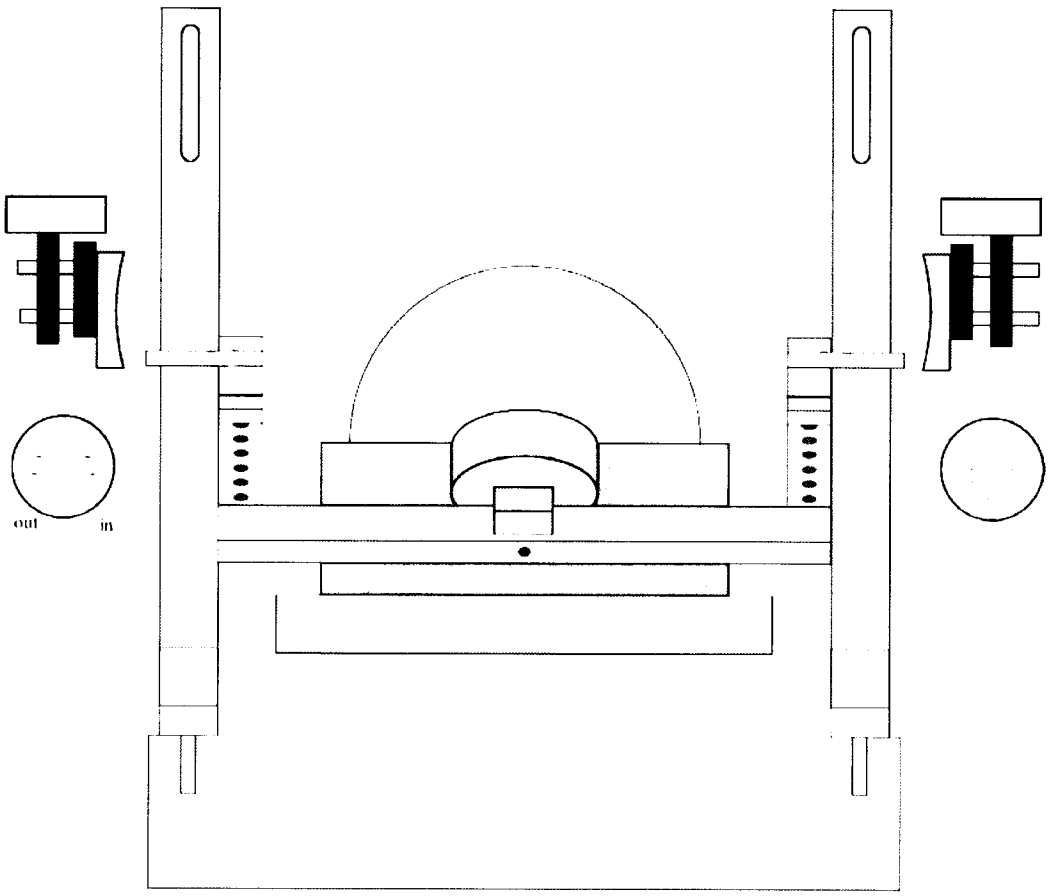

Figure 2.28 Front view of the laser multipass, molecular beam, and liquid surface in the $\varphi_{laser} = 90°$ configuration.

pressure of the system is 2.0×10^{-6} Torr. The diffusion pump is used in all scattering studies to ensure the measurement reflect nascent distributions. Typical operating conditions include pulsed valve repetition rates of 11 – 17 Hz with a stagnation pressure of 100 Torr. In this environment, the average pressure in the chamber reaches $\approx 3 \times 10^{-5}$ Torr, which corresponds to a mean free path of ≈ 500 cm for CO_2.

Within the chamber, the pulsed valve and liquid surface assembly are mounted on a scaffolding stage that is illustrated in Figures 2.27 – 2.32. The stage

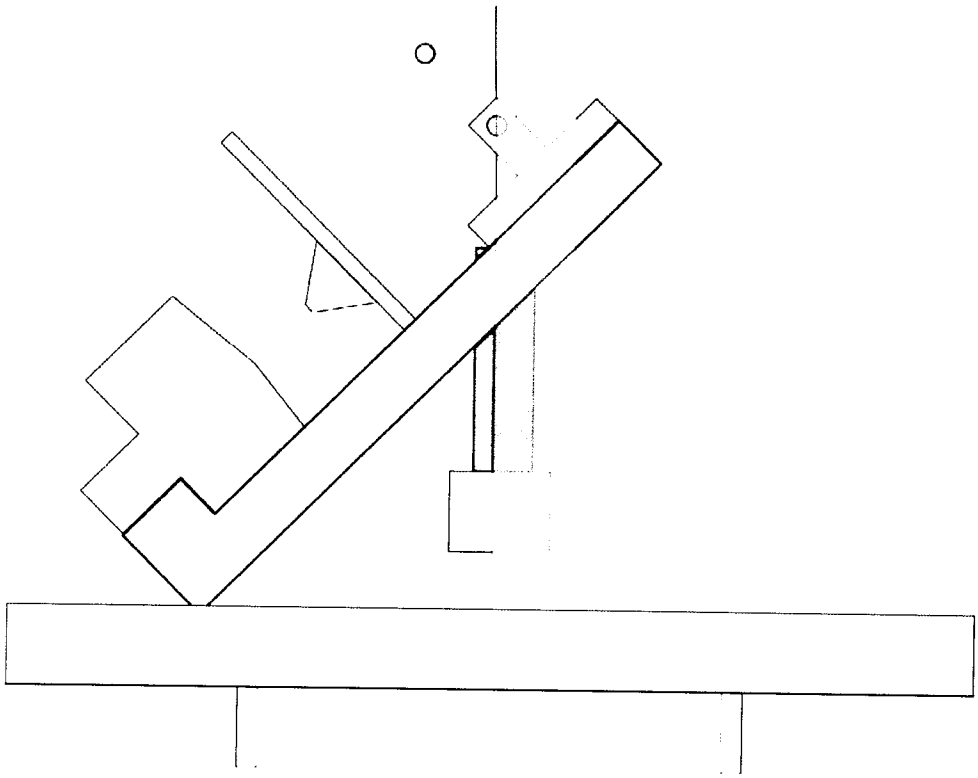

Figure 2.29 Side view of the laser multipass, molecular beam, and liquid surface in the $\varphi_{laser} = 90°$ configuration.

provides the flexibility to measure scattered CO_2 in the two configurations illustrated in Figure 2.27, i.e. $\varphi_{laser} = 0°$ and 90°. In general, the laser beam path remains stationary in each experimental configuration, which then requires a certain degree of mobility for the gas source and wheel components to cover the full range of incident

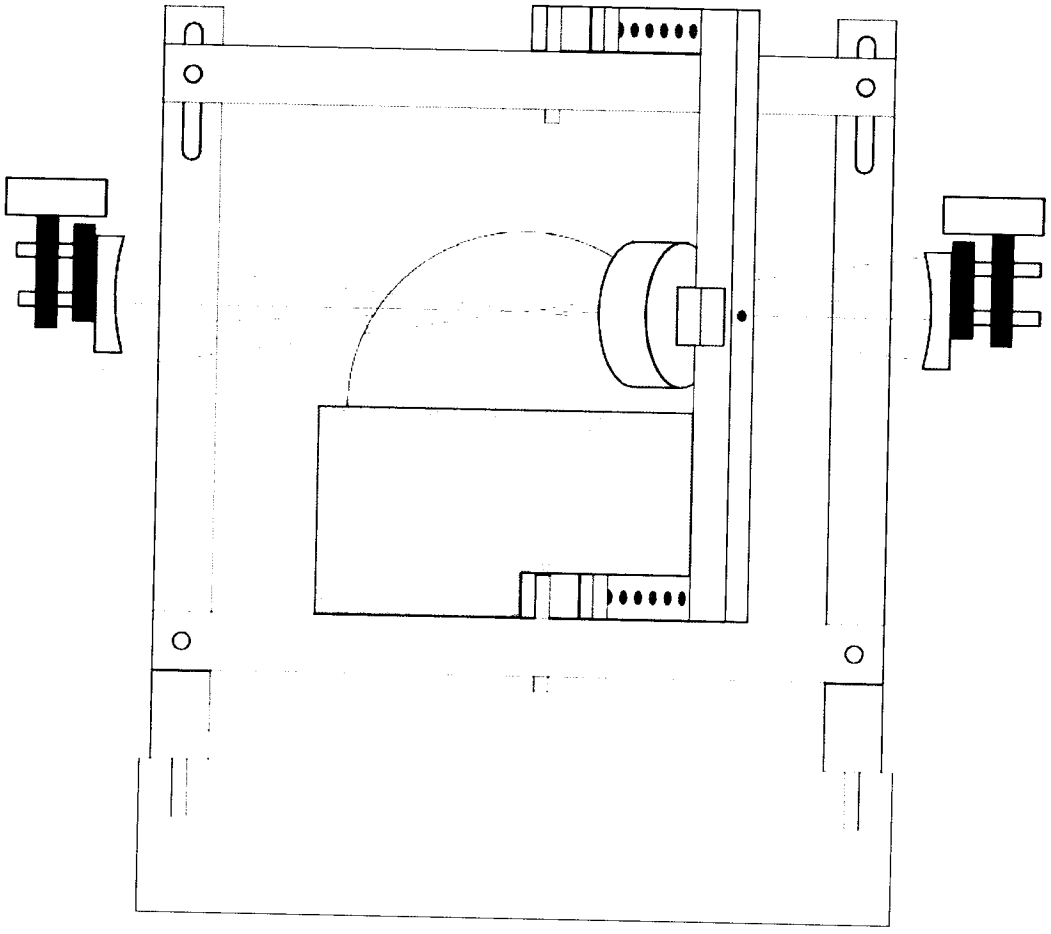

Figure 2.30 Front view of the laser multipass, molecular beam, and liquid surface in the $\varphi_{laser} = 0^{o}$ configuration.

and final scattering angles. The infrastructure is based on two vertical posts that are mounted on rails fixed to the opposite edges of the chamber. These posts not only provide the structural support for the pulsed valve and wheel assembly, but also define the plane of the surface along the front two faces. The rail system is constructed from two plates with a combination of thru holes that enable the posts to translate toward or away from the laser beam in ¼" increments. This flexibility is used to define the final scattering angle for a particular experimental configuration.

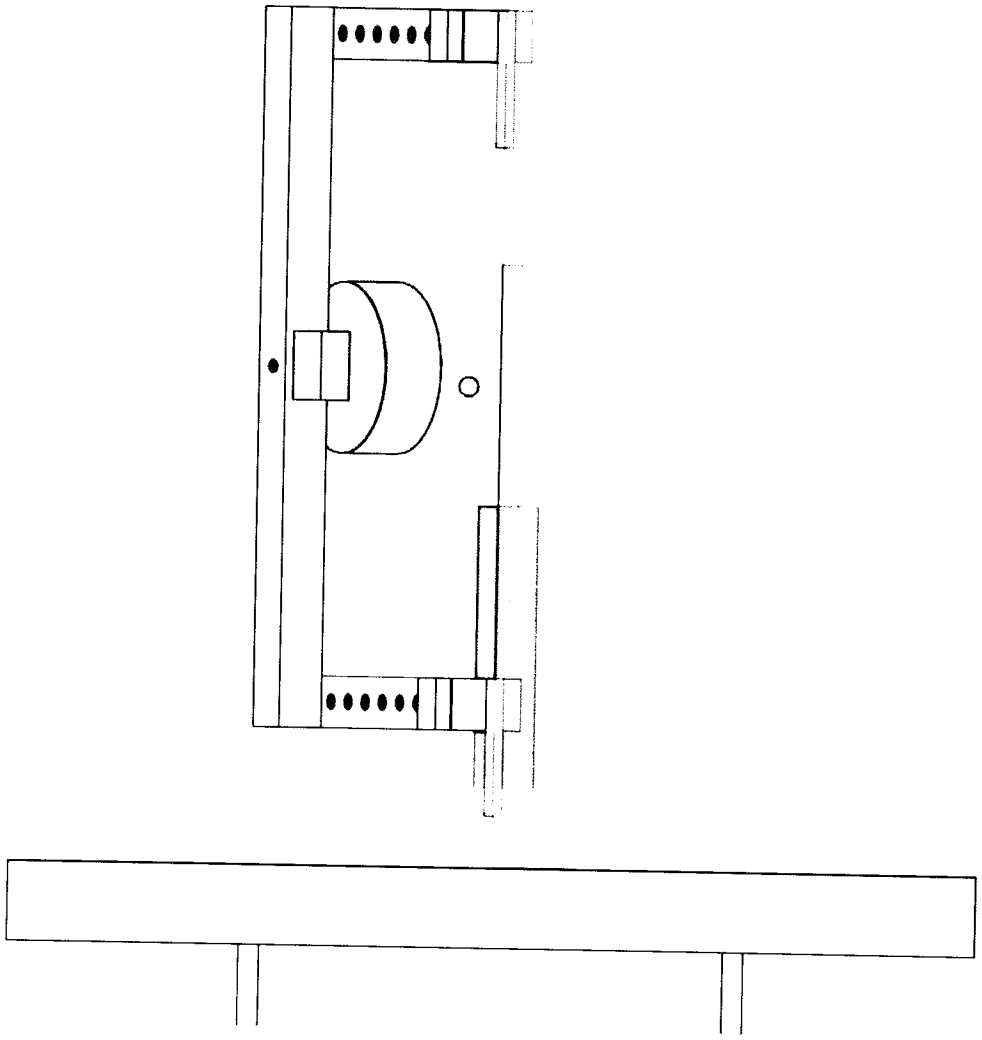

Figure 2.31 Side view of the laser multipass, molecular beam, and liquid surface in the $\varphi_{laser} = 0°$ configuration.

For both φ_{laser} configurations, the posts are initially positioned with an alignment tool that is illustrated in Figure 2.32. The tool is a plexiglass protractor that has been attached to an aluminum "T", which can be clamped at any height to the front faces of the two posts. The opaque transparency of the protractor indicates the position of the center of the HeNe beam in the multipass with respect to the plane of the surface.

To setup an experiment in the $\varphi_{laser} = 90°$ configuration, the protractor is moved into place by adjusting the posts (forward or backward) and tee (up or down) so that the HeNe beam is aligned with markings on the plexiglass at the desired θ_{scat} angle. For most experiments, the center of the multipass is fixed 2.0–2.2 cm from the origin of the protractor, which is used to define the point where the molecular beam expansion axis intersects the surface. The time-of-flight experiments in Chapter 9 require longer surface-to-laser distances, where the physical constraint of the components inside the chamber places an upper limit of $\approx$ 8 cm. Once the protractor is situated, the posts and rails are securely fixed to the chamber, and the positions of the two posts are checked to ensure the laser beam is parallel to the plane of the surface. With the protractor tool in place, the molecular beam is mounted on a "U" shaped boom that is attached to the two main posts with ¼" locating pins on either side. As illustrated in Figure 2.29, the boom pivots around a line that is fixed in the plane of the liquid surface. This configuration constrains the distance between the pinhole and surface at 11 cm for each incident angle. The setup continues with the help of a laser-alignment tool that is mounted in place of the pulsed valve. The locating pins are moved up or down so the light travels through the origin along the desired θ_{inc}. Once the incident path has been established, the boom is fixed in place

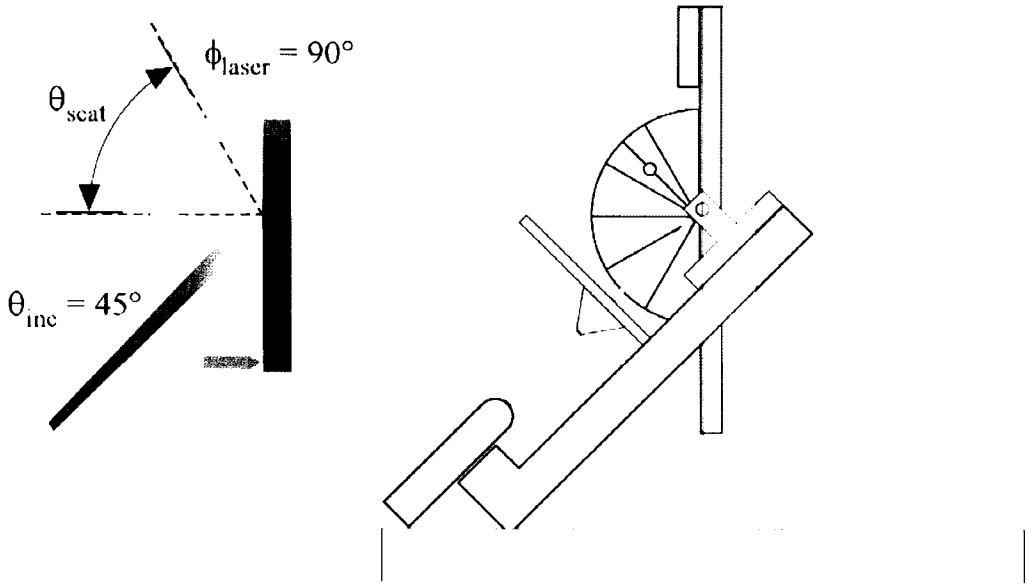

Figure 2.32 Initial setup of the pulsed valve, skimmer, and glass wheel involves an alignment laser and plexiglass protractor.

with an assortment of brackets and side posts. In many of the configurations, the locating pins and adapters must be removed so as not to clip the infrared laser beam in the multipass. Once this path has been cleared, the valve and skimmer plate are reattached to the boom before the experiment.

Setup for experiments in the $\varphi_{laser} = 0°$ configuration start with the HeNe spot near $\theta_{scat} = 0°$ on the alignment protractor. The laser is positioned $\approx$ 1 cm from the surface, where the compact configuration is necessary for glancing incident angles. As illustrated in Figures 2.30 and 2.31, the same U-shaped boom is used to mount the

pulsed valve off two additional rails that have been attached to the main posts. These additional rails may be translated up and down so that the molecular beam expansion axis intersects with the center of the laser multipass. The laser alignment tool is once again used to help set the height of the valve with respect to the IR laser. The locating pins placed so that the pulsed valve rotates around a point on the plane of the surface. The boom is locked in place at the desired incident angle with brackets attached to various part of the scaffolding. The bottom arm of the boom is replaced with a shortened version that allows the liquid wheel reservoir to be fixed in the correct position. In this setup, the skimmer plate is reconfigured to minimize the physical interference with the laser in the multipass.

Once the valve has been positioned for either φ_{laser} configuration, parts of the liquid wheel assembly are added to the chamber, where the location is once again determined with the protractor alignment tool in place of the glass wheel. The assembly design involves a glass wheel that is fixed at its center to an axel, which is mounted parallel to the floor of the chamber with two ball bearings on a vertical post. The bearings slide up and down the post to help position the axel at the correct height. In addition, the post is mounted to the chamber with a bracket that allows translation left, right, forward, or backward. The axel (and subsequently the wheel) is positioned by first marking the spot where the laser alignment tool hits the aluminum tee; i.e. the origin. The height of the axel is first set so that the molecular beam strikes the glass wheel on a spot that is $\approx$ half way from the edge of the wheel to its center. Then, the front face of the axel is positioned flush against the back of the alignment tee. At this point, the brackets are tightened and the protractor alignment tool is removed.

The final steps involve the addition of the liquid reservoir and glass wheel. The reservoir is a copper sleeve, which is placed inside a holder fixed to the back of the two superstructure posts. In the temperature studies, the reservoir is placed inside a temperature-controlled sleeve as illustrated in Figure 2.1. The copper tubing in the sleeve is connected to a Lauda closed-loop circulator with Polyflo tubing. Once the reservoir is secure, the wheel is bolted to the axel so that the front surface is now aligned in the plane defined by the two posts. A razor blade is attached to a holder that fixed to the front edge of the reservoir. Once the wheel is setup, a gear on the far side axel is attached to drive system that is designed to rotate the wheel through the reservoir. The gear is coupled to two additional gears; (i) the first is directly attached to a 30 VDC motor through a ferrofluidic feedthrough, and (ii) the second is used to add tension to the rubber drive belt that connects all three. The motor is mounted to the external side of the flange, where a series of gears and bicycle chain provide the necessary mechanical flexibility. The motor is connected to a power supply through a voltage divider that provides course control of the rotational speed.

2.4.2 Liquid Surface and Characterization

The primary reason for the liquid wheel assembly is to expose a renewed liquid surface for the incident molecular beam. The ways in which these surfaces have been characterized in previous studies involves neutron and Ar^+ scattering to show that the liquid is relatively clean. In addition to these techniques, simple surface tension measurements are an easy and reliable method to characterize the impurities on the liquid. The general technique involves the Wilhelmy plate method that extracts the surface tension from the measured force required to pull a paper plate out

of the liquid. Equipment for these types of experiments has been developed by companies like NIMA that specialize in Langmuir-Blodgett (LB) troughs for precise surface pressure measurements. The honors general chemistry course at CU includes a lab that explores surface tension with experiments that involve troughs and sensors, which have been built by the machine shop in Cristol Chemistry. Fortunately, the shop built an extra setup that was then carefully moved to B217 in JILA to help characterize the liquid surfaces. The equipment includes a LB trough and sensor that are computer controlled through a serial connection with NIMA interface electronics. Detailed user instructions have been provided, so the general operating procedure is simply outlined in the following few paragraphs.

The surface tension measurements are made with a sensor that is designed to measure force on a lever arm connected to an electric motor. Servo loop electronics adjust the current to the motor to keep the position of the lever arm constant with increasing or decreasing forces. The key to the measurement is that current through the motor is directly proportional to the force on the lever arm. The NIMA interface converts this current to a voltage that can be read through a serial connection on a computer. Based on this scheme, the sensor is used to measure the force exerted on a plate by the surface. To do this, the sensor is first calibrated with a series of known weights that range from 1 – 100 grams. Once calibrated, a clean paper plate (10 mm wide, 0.25 mm thick) is attached to the lever arm, at which point it is dipped into the liquid to the point where the paper is thoroughly wetted. The forces on the plate include gravity and surface tension pulling down and buoyancy pushing up. Gravitational forces remain constant throughout the measurement, which simply leads

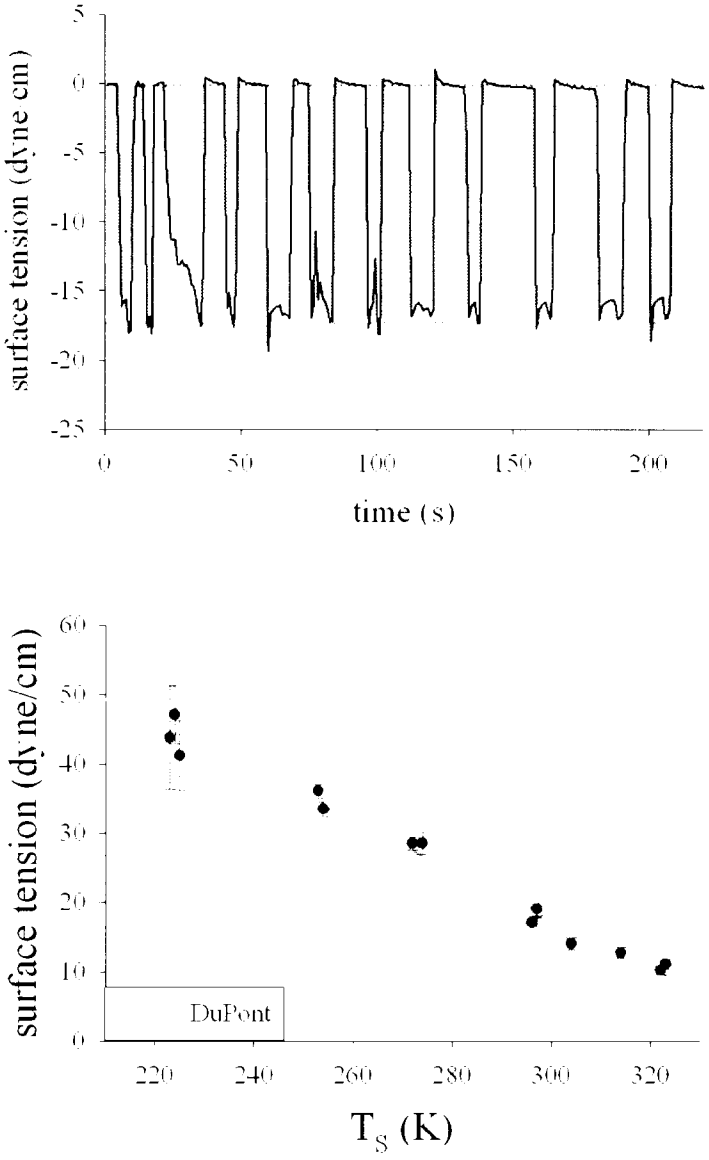

Figure 2.33 Surface tension of PFPE is measured as a function of temperature.

to a constant voltage offset that may be zeroed by the computer program. The competition between buoyancy and surface tension are monitored as a function of time as the plate is pulled from the liquid. Once the paper is out of the liquid, the only force is surface tension on the perimeter of the plate since the buoyancy term drops to zero. The force is recorded as plate is finally pulled free of the liquid, where the difference is equal to 2 × *width* × *thickness* × surface tension. Therefore, the dimensions of the plate lead directly to the surface tension. Sample time traces of the surface tension are illustrated in Figure 2.33 (top) for PFPE at 298 K. The dotted lines correspond to average difference between steps that result from the repeated measurements with the same plate. The temperature dependence of the surface tension is illustrated in Figure 2.33 (bottom), where the data also includes the value from the Krytox specification sheet from DuPont. In general, an aliquot of liquid is transferred to a clean Petri dish for analysis because direct access to the reservoir is a technical challenge. Measurements have been made before and after many experiments to ensure the setup guarantees a freshly renewed and clean liquid surface.

2.4.3 SAM chamber

Further scattering experiments have been planned to explore other realms of gas-surface interactions. The first series of experiments involve surfaces of self-assembled monolayers (SAMs) that are generated from alkane thiols and clean gold substrates. To help ensure the cleanliness of a sample, a vacuum chamber has been built with turbomolecular pumps that are designed to eliminate the presence of

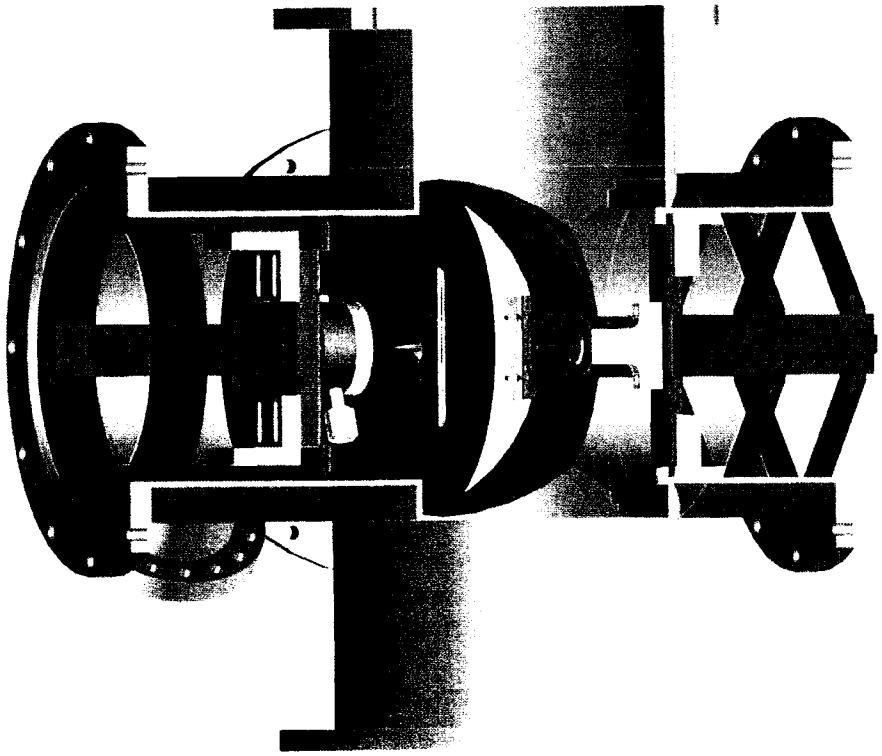

Figure 2.34 Gas + SAMs scattering chamber includes a differentially-pumped source volume within the main scattering chamber.

background oils. A cartoon cross-section of the chamber is illustrated in Figure 2.34 to show the essential components. The chamber is based on a modified six-way cross (Nor-Cal) that is constructed from 10" tubes of stainless steel. The modifications include additional length on two arms and side ports for differential pumping. The chamber is attached to a base plate on an aluminum support frame, which stands on the ground with rubber feet for vibration isolation. The main turbo pump (Pfeiffer TPH 1201) is also attached to the bottom of the base plate through an ISO 200 o-ring

seal. This pump is backed by a second Edwards E2M30 rotary vane pump through stainless steel bellows. The chamber is divided into two parts, source and scattering, by an insert constructed in the JILA machine shop. The source region contains the pulsed valve and skimmer, while the scattering chamber houses a sample holder and multipass optics. Fully assembled, the chamber reaches a base pressure of 2×10^{-8} Torr with both pumps operating. Further descriptions of the components are outlined in the following paragraphs.

The chamber design incorporates a differential pumping scheme to reduce to the background gas in the scattering chamber. The pulsed valve is mounted in one arm of the six-way cross, which is then partitioned from the remaining part of the chamber through the differential insert illustrated in Figure 2.35. The insert is constructed from two main rings that are connected by four support rails. These rails also include tapped ¼-20 thru holes to mount various components inside this region of the chamber. The two rings are assembled before being positioned in the main chamber. Once inside, each ring has four threaded holes for 5/16-18 grub screws that are used to center and secure the ring inside the tube. Once these screws are extended, the pressure on the outside wall locks the differential insert into place. To seal the insert from the rest of the chamber, a thick o-ring is wedged between the outer wall of the chamber and a beveled edge of the inner aluminum ring. The inset in Figure 2.35 illustrates the seal, where a secondary outer ring is bolted to the main insert to compress the o-ring between the two surfaces. This secondary ring also has a series of threaded holes for additional bolts that may be used to close the larger gaps around the ring. Once setup, the o-ring seal is checked first with light to visibly

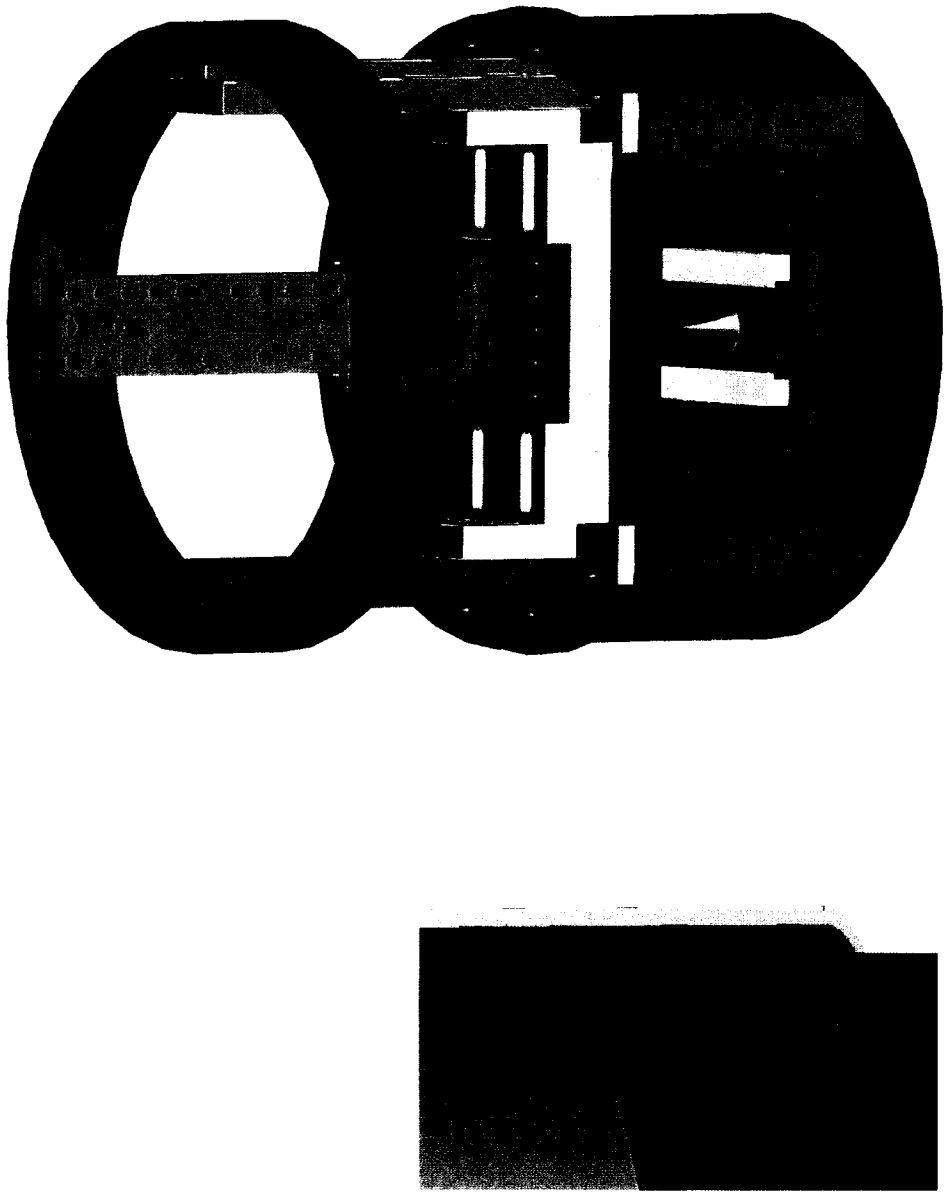

Figure 2.35 Differential insert for the source chamber includes scaffolding to mount the pulsed valve and flexible skimmer plate. The insert is sealed from the scattering chamber with an oversized o-ring and compression ring, which is illustrated in the bottom inset.

observe any gaps that would lead to leaks between the source and scattering chambers.

The two other features in the source chamber include mounts for the pulse valve and skimmer. Initial studies have involved a second PZT valve, which is mounted to the brackets illustrated in Figure 2.35. These brackets translate vertically to increase the range of incident angles in the scattering experiment. Additional brackets have been machined to securely mount an Even-Lavie valve if shorter gas pulses are required. The plate at the end of the insert is attached to the inner ring with an o-ring seal. A hole in this plate may either be covered with a skimmer or left open for direct throughput for the gas from the skimmer. The skimmer is mounted on two plates that provide vertical and horizontal translation to match the mobility of the PZT valve. These plates are clamped together and sealed by o-rings. The source region of the chamber is pumped through one or two side ports that have been welded to the side arm of the six-way cross. An Edwards turbo pump (EXT 250) is attached to one of the ports, which is then backed by an Edward E2M18 rotary vane mechanical pump. A second port provides access for a second pump if greater speeds are required. This section of the cross is sealed with a ISO 250 aluminum flange with throughputs for gas, power, thermocouple and ion gauges, and a vent valve that is attached to a tank of N_2.

The scattering chamber includes a scaffolding structure that is used to mount the sample. Details of this construction are depicted in Figure 2.36, which shows the sample holder and support structure that is attached to the internal frame. The sample holder is designed to support a 1" × 3" gold slide, where the entire mount may

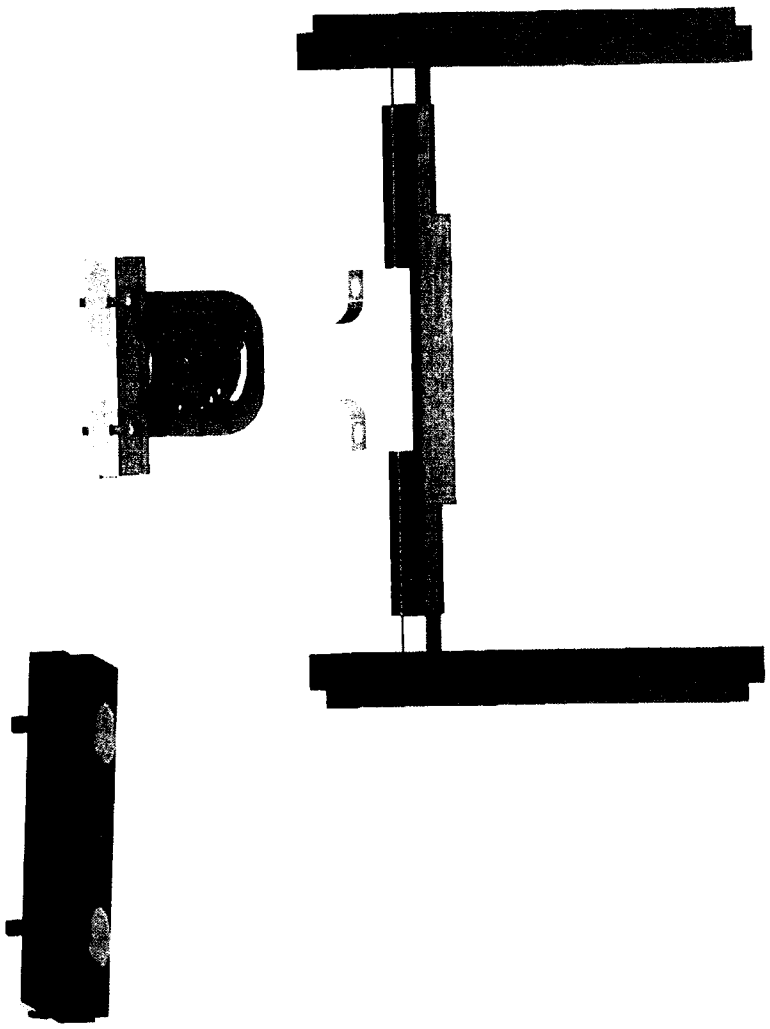

Figure 2.36 Surface samples are mounted on a holder in the opposite arm of the six-way cross source chamber.

be rotated in 15° increments to change in the incident scattering angles. The entire sample may be translated with respect to the laser beam to change in final scattering angle. The laser is passed into the chamber through CaF_2 windows onto gold mirrors in a multipass configuration. The mirrors are mounted on an adapter with a setscrew so that no glue introduced to the chamber. These adapters fit in a standard 1" Newport Suprema optics mount that is attached to the stainless steel side flanges. The actuators for these mounts are controlled through Ultra-torr feedthroughs that have been welded to the stainless steel side flanges.

2.5 Polarization Modulation

2.5.1 Experimental Setup

The basic components of the spectrometer are kept in place for the stereodynamic studies in Chapters 10 and 11. Several modifications and additional components are necessary to control the polarization of the laser light. First, the 50/50 beam splitter that normally divides the light between signal and reference InSb detectors is replaced with a gold mirror so that all light is passed into the chamber. The reason involves the additional losses to the laser power that result from the Rochon polarizer (Karl Lambrecht, MFRV9) and photoelastic modulator (Hinds International, PEM-80 ZS). The positions of these components are illustrated in Figure 2.37. The polarizer spatially separates the two polarizations with MgF_2

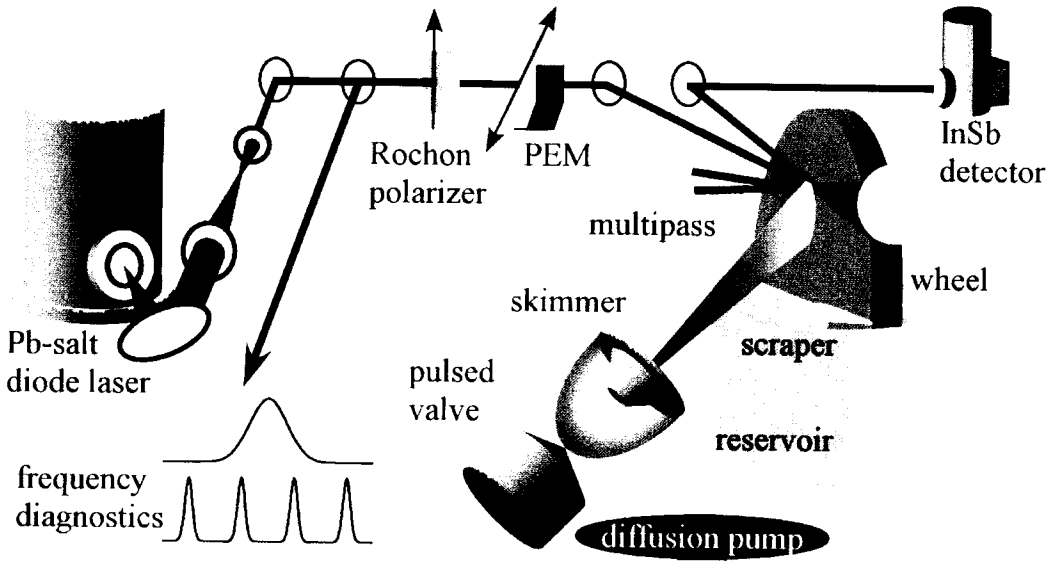

Figure 2.37 Stereodynamics are measured with polarization modulation of the laser light and lock-in detection.

crystals that redirect one of the linear components away from the initial laser propagation vector. With the Polarization axis set perpendicular to the laser table, the transmitted light corresponds to ≈81% of the total power, which indicates the light from the diode laser is elliptically polarized to a degree. As a test, a second Rochon polarizer is used in a cross-configuration, which then attenuates more than 99.8% of the light. Additional losses include reflection from the MgF_2 ($n = 1.35$ at $\lambda = 4.2\mu m$) and PEM, which is constructed from a ZnSe crystal ($n = 2.43$ at $\lambda = 4.2\mu m$). The losses from reflection and initial polarizer lead to ≈43% transmission of the initial power. Since the diode output is ≈ 1 μW or less, the second beam splitter is omitted so that higher laser power may be used to detect the alignment and orientation signals.

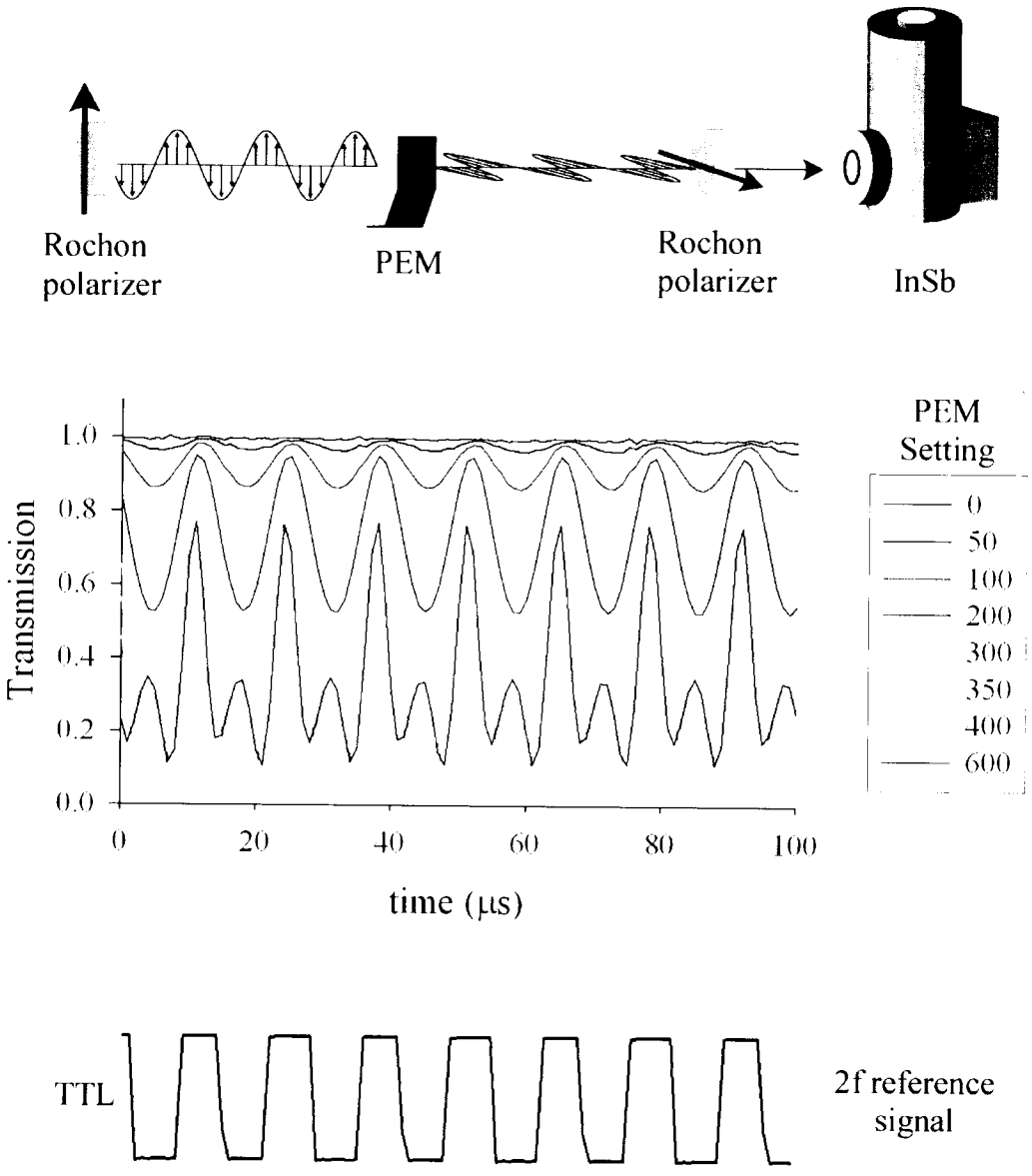

Figure 2.38 A photoelastic modulator (PEM) is used to rotate the polarization from parallel (||) to perpendicular (⊥) or from right (RCP) to left circular (LCP). The amplitude of the PEM oscillation is optimized by passing the rotating light through a second cross-configured Rochon polarizer. A reference signal from the PEM controller is used in a standard lock-in detection scheme.

The initial setup involves first overlapping the IR and HeNe beam through two irises that span the width of the laser table. The beams are then aligned into the multipass to establish the detection axis for the scattering configurations. Two additional irises are placed in front of the chamber to mark the laser path into the chamber. Next, the Rochon polarizer and PEM are mounted in between the first two irises that were used to overlap the beams. The polarizer is fixed in place so that the polarization vector for the transmitted light is perpendicular to the laser table. Next, the PEM is mounted so the beam passes through the center of the ZnSe crystal. The PEM is designed to rotate the polarization vector through stress induced birefringence along one of two crystal axes. Two piezoelectric bars are glued to opposite edges of the eight-sided crystal. These bars define the primary axis of the crystal, which is then aligned at 45° with respect to the polarization vector from the Rochon crystal. These two components tend to shift the beam path slightly so that the initial alignment of the Herriot cell multipass is lost. To reestablish the defined path through the chamber, turning mirrors are used to realign the HeNe and IR beams through the two irises that were placed at the entrance to the multipass optics.

The piezoelectric transducers in the PEM are driven with a 37.5 kHz sinusoidal voltage from a high voltage controller. When the crystal oscillates, the material is either stretched or compressed along the principle axis, which leads to birefringence in this direction. When the light is passed through the PEM, the birefringence causes a phase shift of the electric field component along the principle axis. The magnitude of this effect is controlled by the amplitude of the crystal oscillation. As the driving voltage increases from zero, the polarization of light is

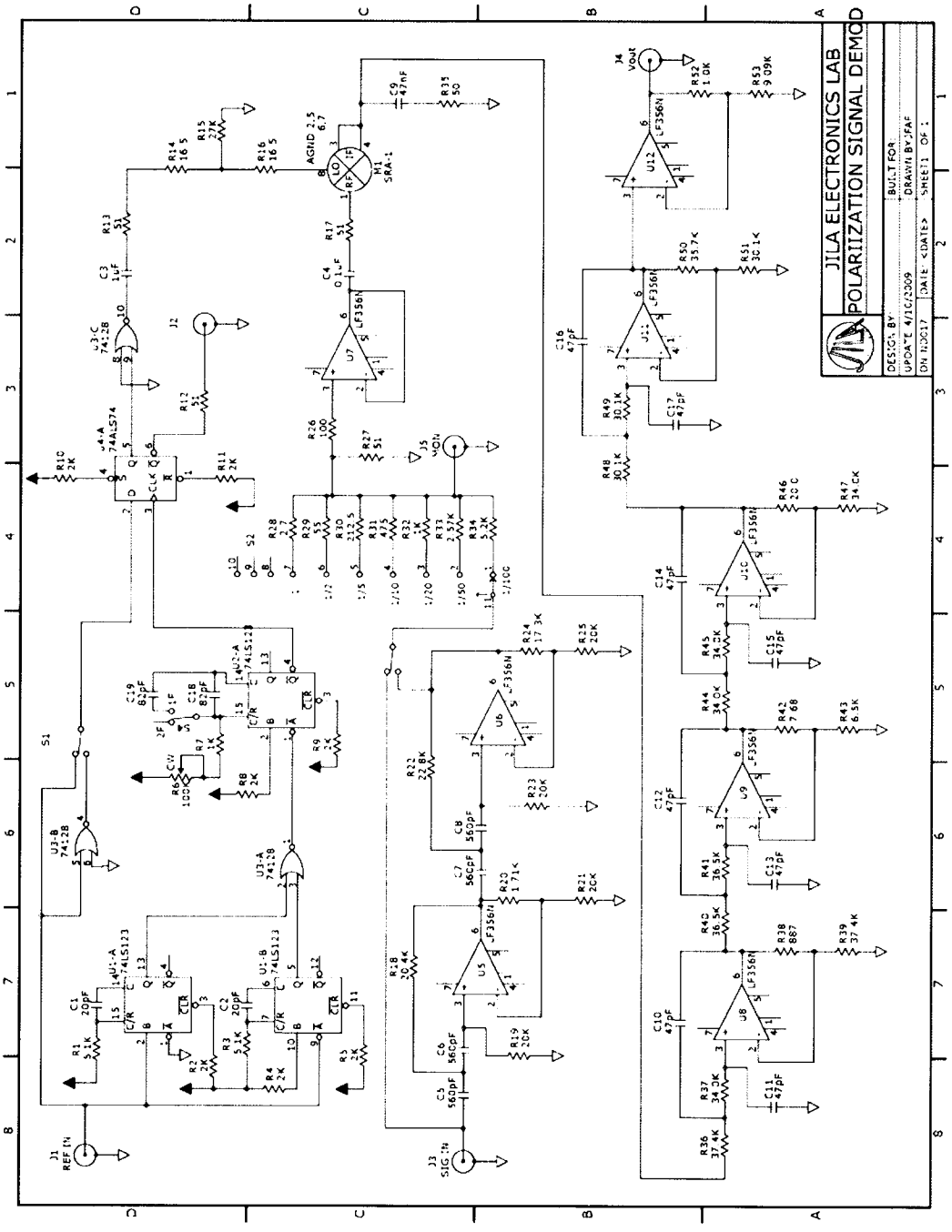

Figure 2.39 Polarization signal demodulator.

rotated from linear to elliptical. At some point, the phase shift reaches 90°, which creates oscillating circularly polarized light at 37.5 kHz. Eventually, the phase shift reaches 180° to generate the orthogonal linear state at twice the driving frequency, i.e. 75 kHz.

The amplitude of the PEM is set by passing the rotating light through a second Rochon polarizer, which may be configured in either a cross or parallel configuration. The setup is illustrated in Figure 2.38, along with sample time traces from a parallel-configuration calibration. The plot shows that the transmission through the 2nd polarizer is 100% with the PEM driver off. As the PEM is turned on, a 75 kHz sine wave is observed as the oscillation amplitude drives the birefringence in the crystal. The magnitude of the sine wave time trace increases with the voltage, which is varied by a dial on the PEM controller. The maximum amplitude of this signal corresponds to linear polarized light with the orthogonal polarization. As the voltage increases past this value, the phase between the two polarizations shifts beyond 180°, which shows up as an additional 75 kHz component in the time trace. Experiments with oscillating linear polarizations involved fixing the PEM dial at 400. Calibration of the oscillating circular polarizations involves passing the light through a MgF_2 Babinet-Soleil compensator (Karl Lambrecht, BSMF-13-2) before the 2nd Rochon polarizer. The BS compensator acts as a ¼-waveplate to turn circular into linear polarization. The transmitted light once again oscillates at 75kHz, but the maximum signal corresponds to circular polarizations. For these experiments, the dial reading was fixed at 163 on the PEM controller.

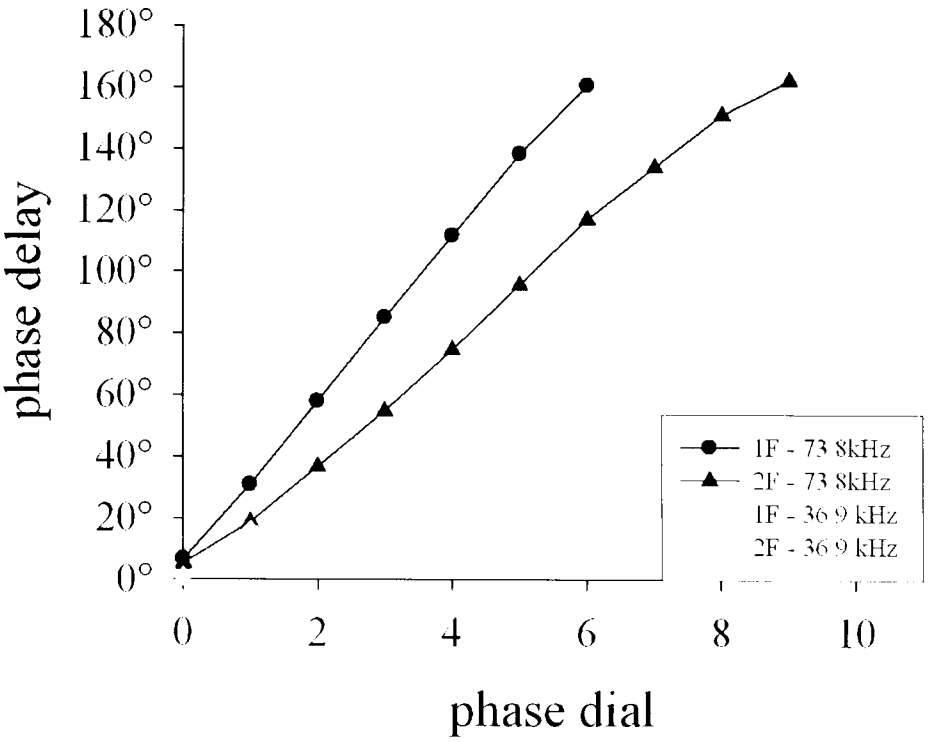

Figure 2.40 Phase calibration curves.

Table 2.2 Phase demodulator calibration.

Dial	1F (73.8 kHz)	2F (73.8 kHz)	1F (36.9 kHz)	2F (36.9 kHz)
0.00	6.65°	5.32°	1.06°	0.80°
1.00	30.84°	18.61°	15.95°	10.63°
2.00	57.95°	36.68°	28.44°	18.61°
3.00	80.06°	54.76°	42.53°	27.65°
4.00	111.65°	74.70°	58.48°	37.22°
5.00	138.23°	95.70°	73.10°	47.85°
6.00	160.56°	116.96°	89.32°	59.01°
7.00		133.98°	102.34°	71.24°
8.00		150.98°	119.62°	82.41°
9.00		162.15°	134.24°	93.04°
10.00			146.20°	98.35°

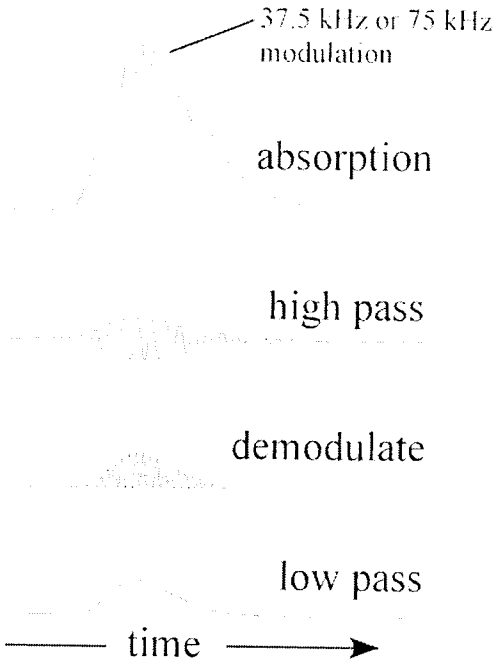

Figure 2.41 Sample absorption and demodulated signals.

2.5.2 Signal Processing and Analysis

Voltages from the signal InSb detector are split so that one fraction is sent directly to the computer A/D (PCI-6110E, Channel 0), while the other is demodulated in the circuit outlined in Figure 2.39. The home-built signal demodulator is designed as a standard lock-in that rectifies the signal voltage by heterodyning it against a reference signal from the PEM controller box. The correct phase between the signal and reference voltages is set in the following way. Light with oscillating

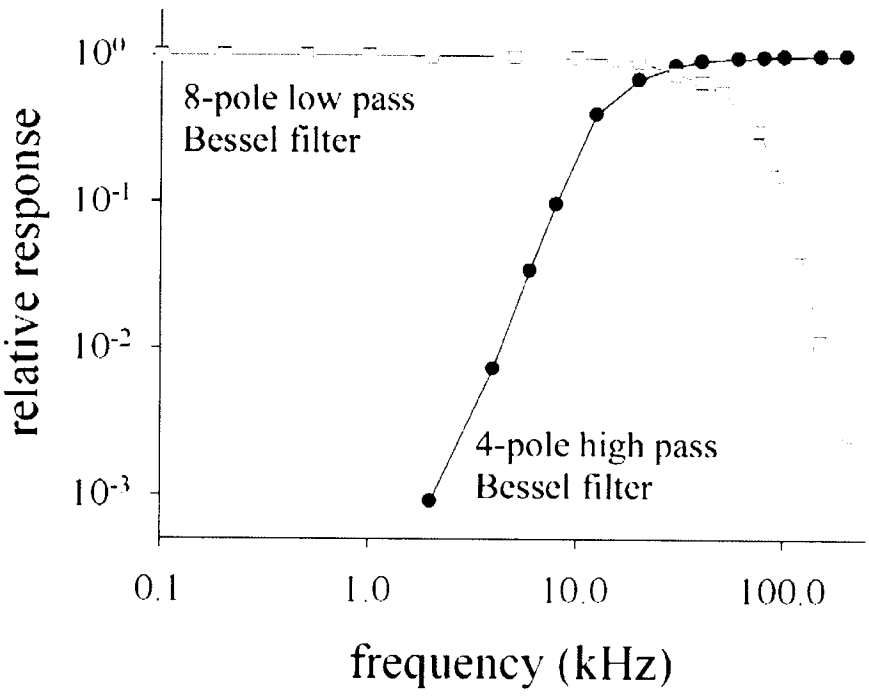

Figure 2.42 Bandwidth of the active high and low pass Bessel filters in the polarization signal demodulator.

polarizations from the PEM is once again passed through a cross-configured Rochon polarizer to generate a sine-wave at the correct frequency. This signal is passed into the demodulator circuit, at which point the phase control is used to null the output. The phase is recorded, and then shifted 90° using interpolated values from a known calibration. Values for this curve are plotted in Figure 2.40 and listed in Table 2.2 for the various f and 2f settings.

Output voltages from the signal demodulator are sent to Channel 1 of the A/D to be stored in parallel with the absorbance traces. A simulated time traces are plotted in Figure 2.41 to show the sequence of signal manipulation through the

experiment. The absorption signal for each quantum state transition corresponds to the value $(A_{RCP} + A_{LCP})/2$ or $(A_{\parallel} + A_{\perp})/2$. This signal is filtered with a 4-pole high-pass Bessel filter to isolate the modulated components of the signal. The bandwidth of this filter is plotted in Figure 2.42. Once filtered, the signal is rectified and then passed through an 8-pole low pass Bessel filter to remove the 2f component. The resulting time trace of the demodulated signal is proportional to either $A_{RCP} - A_{LCP}$ or $A_{\parallel} - A_{\perp}$. Appropriate characterization of the circuit provides the necessary gain factors that are used to turn the raw voltages into differential absorbances. The data is analyzed in a program called *alignment.c*. One additional comment about the signals is well-explained in Miles Weida's thesis. Stray birefringence in the optical path leads to spurious signals that can alter the magnitude, and even the sign of the demodulated signal. These effects are taken into account within the analysis program since the absorbance is recorded in parallel with the demodulated signal.

2.6 Data collection and analysis

2.6.1 Experimental Interface

The experiment is computer-controlled through two National Instruments data acquisition cards that provide an interface between hardware and software. A C-based program called *scan4.c* has been written in the CVI programming platform to run the experiment through these two data acquisition boards. The source code for *scan4.c* is included in Appendix D. The DAQ cards are equipped with timing functions that are used to control standard analog and digital input/output to the

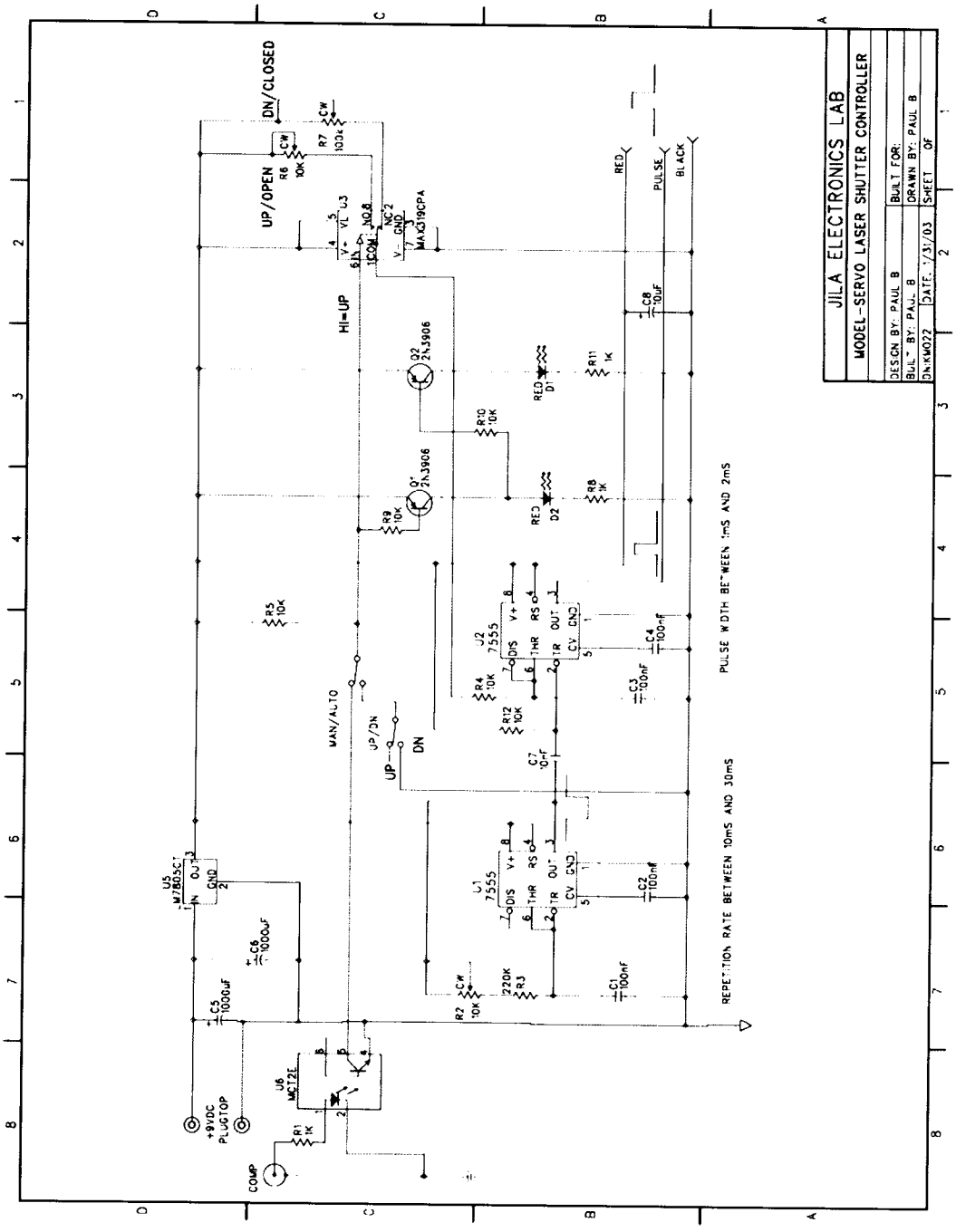

Figure 2.43 Remote-controlled shutter electronics.

experiment. The first DAQ card (PCI-6110E) includes four 12-bit analog-to-digital (A/D) converters that sample input voltages (–10 to +10 V) at a maximum rate of 5 MHz over the four channels. One of these A/Ds is used to record the voltages from the signal subtraction electronics and, if necessary, a second channel records voltages from the polarization demodulator in the stereodynamics studies. The board also includes two 16-bit analog outputs, one of which is used to scan the laser after a transient absorption signal has been recorded at a particular frequency. In addition, a TTL voltage from a general counter on the board is used to trigger the pulsed valve. The second DAQ board (PCI-6025E) is used to perform a variety of additional functions in the experiment. The card has eight A/Ds that sample voltages (–10 to +10 V) at 200 kHz with 12-bit resolution. These channels are used to record signals from the etalon and reference gas cell detectors, DC powers from the signal and reference InSb detectors, and stagnation pressure in the pulsed valve. One of the analog outputs on the 6025E card also triggers a remote-controlled laser shutter that is used at the end of the scan to determine the laser power levels on each detector for the conversion to absorbance. The schematic for the shutter controller is printed in Figure 2.43

Before each experiment starts, initial efforts include laser alignment, surface preparation, and initiation of the pulse valve. The laser beam is aligned through the multipass while the vacuum is vented to atmosphere. Once the valve and liquid surface have been setup, the flanges are replaced and the system is roughed by a second mechanical pump before the gate valve to the diffusion pump is opened. As the pressure continues to drop, the multipass is realigned since the beam tends to

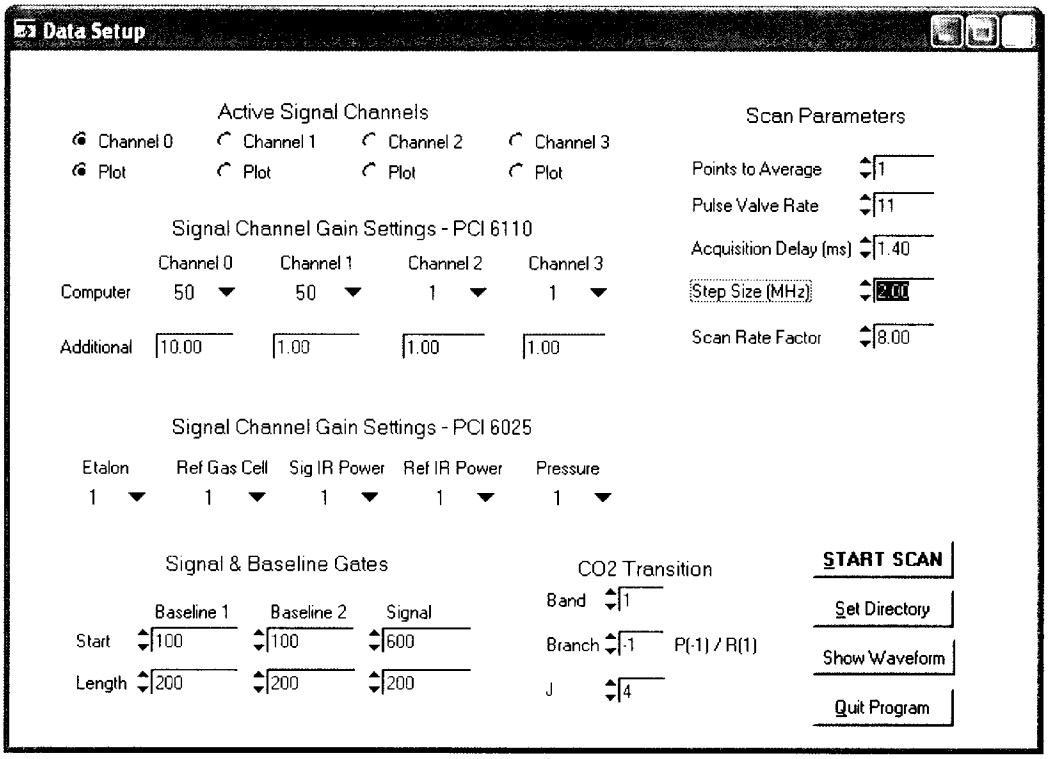

Figure 2.44 Data acquisition interface panel to select scan parameters.

move as the flanges flex and shift the mirrors inside the vacuum. At this point, the purge box is sealed and flushed with N_2 from a 1A tank. As CO_2 is slowly driven from the spectrometer, the scanning program is started to initialize the pulsed valve. Flux through the pinhole is calculated from the measured drop in pressure over time as the valve after the regulator in the gas manifold is closed. These values are used to calculate an effective area of the pinhole, which is then compared to the actual physical area. Close agreement between the two values is expected when the valve is operating correctly. At this point, the liquid on the wheel is visually inspected

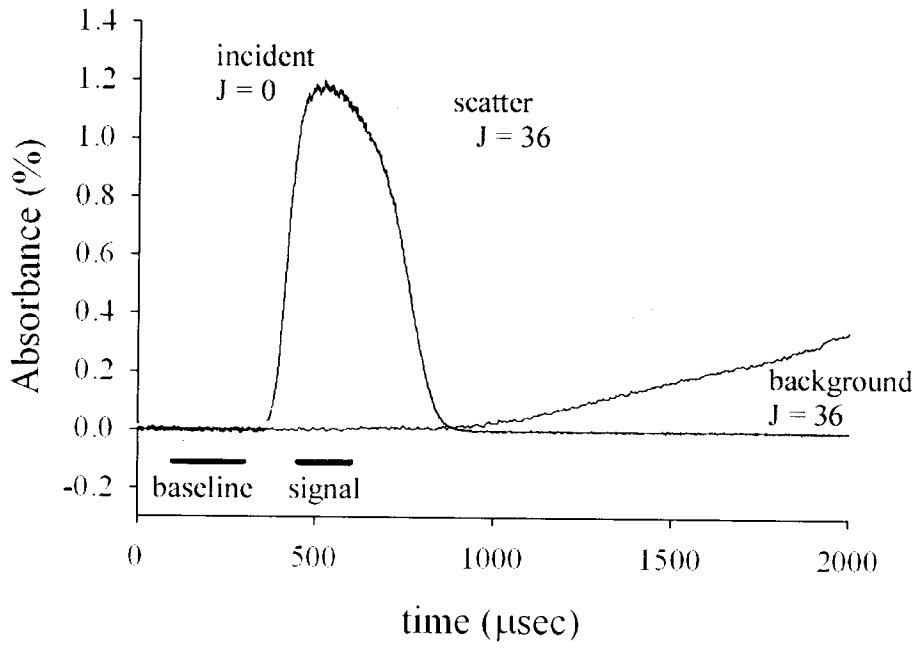

Figure 2.45 Sample time profiles for incident, scattered, and background signals of CO_2 scattering from PFPE liquid surface.

through the plexiglass flange to make certain the coverage and consistency are satisfactory before starting the experiment.

With *scan4.c* running, the laser is tuned to a rovibrational transition and parked ≈ 500 – 1000 MHz below the centerline frequency. The user interface includes the Data Setup window illustrated in Figure 2.44. The panel allows the user to input various control parameters that are used to scan and record data. Most of these values are recorded in the header of each file as it is saved at the end of the scan. The interface requires the user to choose baseline and signal gates that are used to integrate the scattered CO_2 signal. These values are simply used to visually present

Table 2.3 Header information for vscan*date.xxx* files.

C	F77	Variable	Program	Notes
0	1	max_zahl	et.f	Number of transmission fringes
1	2	maxspur	scan4.c	Number of traces
2	3	*u*PulseAve	scan4.c	Pulses averaged per frequency step
3	4	*l*B1Start	scan4.c	Start of baseline 1 gate
4	5	*l*B1Length	scan4.c	Length of baseline 1 gate
5	6	*l*SigStart	scan4.c	Start of signal gate
6	7	*l*SigLength	scan4.c	Length of signal gate
7	8	*l*B2Start	scan4.c	Start of baseline 2 gate
8	9	*l*B2Length	scan4.c	Length of baseline 2 gate
9	10	*ul*PulseRate	scan4.c	Repetition rate for pulsed valve
10	11	*i*counter	scan4.c	Data points per scan
11	12	stagpress	scan4.c	Stagnation pressure
12	13	StoreHour	scan4.c	Hour of scan
13	14	StoreMinute	scan4.c	Minute of scan
14	15	StoreTime	scan4.c	Time of scan
15	16	StoreDate	scan4.c	Date of scan
16	17	iBand	scan4.c	1 ($00^{0}0$), 2 ($01^{1e}0$), 3 ($01^{1f}0$)
17	18	iBranch	scan4.c	P branch (-1), R branch (+1)
18	19	iJState	scan4.c	Rotational State
19	20	sCompGain	scan4.c	Software selected gain
20	21	dOtherGain	scan4.c	Other gain factors
21	22	RefWgau	voigta.f	298 K Doppler width (MHZ)
22	23	Wlor (ref)	voigta.f	Lorentizian line width (ref peak)
23	24	Wlor (sig)	voigta.f	Lorentizian line width (late sig peak)
24	25	Wgau	voigtb.f	Signal Doppler Width (ref $\Delta\nu_{lor}$)
25	26	Wgau	voigtb.f	Signal Doppler Width (sig $\Delta\nu_{lor}$)
26	27	IntAbs1 (sig)	voigtb.f	Signal column density (A*MHz)
27	28	IntAbs1 (ref)	voigtb.f	Reference column density (A*MHz)
...	...	[a]		
...	...			
...	...			

[a]Header variables 28–39 are filled by other programs, such as voigt2.f, vv3.f, and other line shape fitting algorithms.

the data in real time as the laser is scanned over the transition. The program stores the entire time profile (2 ms) at each frequency so that integrated signals from various time windows may be analyzed afterward. Sample time traces are plotted in Figure 2.45 to show typical incident beam, scattered CO_2, and background signals at the centerline frequency. The plot also includes typical windows for the signal gate, which integrates some fraction of the rising edge of the scattered pulse. The scanning program plots absorption versus frequency in a panel displayed in Figure 2.46, which also shows the etalon fringes, reference gas absorption, and DC power on the InSb detector. At the end of the scan, the beam is blocked and 50 points are recorded to provide offset values on each detector. Data is then stored in a format listed in the source code comments in Appendix D, as well as Table 2.3. Absorption profiles are measured three times each for the ground state and hotband transitions that are accessible with the laser diode.

2.6.2 Analysis

Frequency-dependent absorption profiles are generated from the two-dimensional data array in a program called *gate.c*. Signal and base line gates are chosen from initial analysis of the centerline time profiles for a series of ground state transitions. In general, the shape of the time profile depends on the specific rotational state since the translational distributions are sensitive to the quantum-state. Signals from high J-states arrive earlier than those from low J, which creates some confusion about the appropriate integration windows. Profiles for a series of J-states are plotted to reveal the spread in arrival times, at which point the time trace from a middle J-

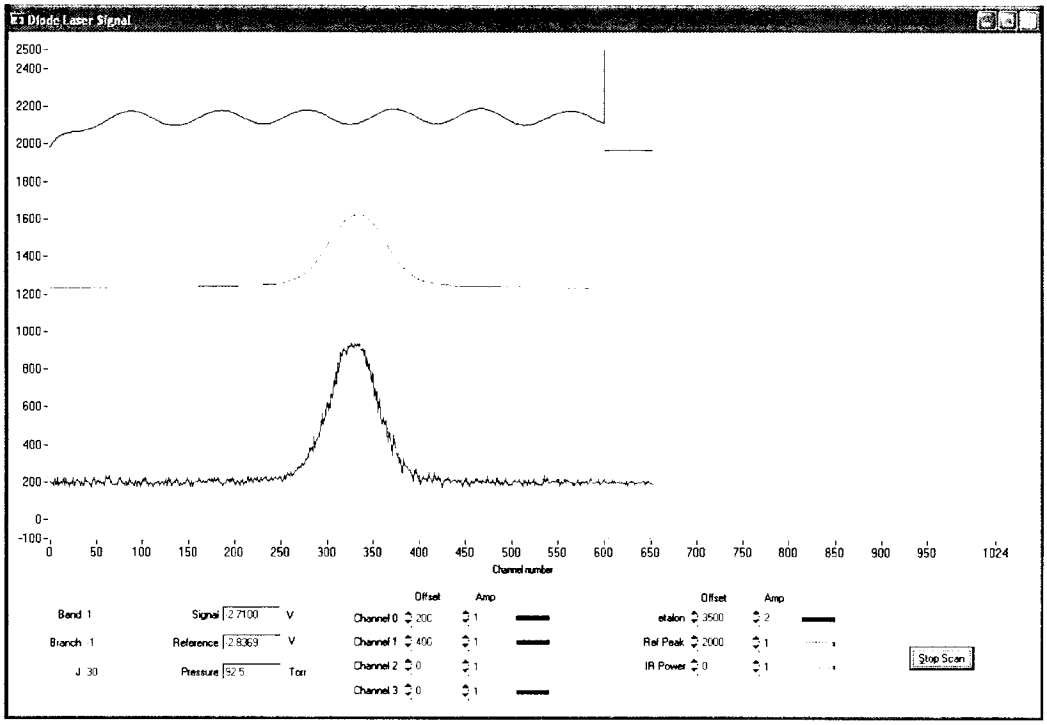

Figure 2.46 Sample frequency trace with scan4.c illustrates absorption profiles for CO_2 in the scattered flux and reference cell, along with the transmission fringes from the etalon.

state is selected to represent the average. From the peak absorbance, the signal integration window is selected to encompass 25–75% of the rising edge for this transition. Such *ad hoc* criteria has been rigorously tested by integrating the time profiles in incremental steps of 100 μsec to show the effects lead to negligible differences in line shapes and relative population distributions. This routine provides a reasonable approach to account for differences in each experimental configuration. The rising edge of the transient scattered signal is selected to minimize the contamination by background CO_2, which often lead to relatively large absorbance signals because the laser is passed across the width of the entire chamber multiple

times in the Herriot cell. These files are saved as *scanDATEb.xxx*, where DATE is a 4-digit month/day and *xxx* is a file listing from 001 to 999. In addition to these profiles, signals at the end of the time trace are integrated to show the resulting Doppler profiles lead to room temperature rotational and translational distributions. These files are saved as *scanDATEa.xxx*.

Once absorption profiles have been generated, the analysis continues by first interpolating between the transmission fringes to provide accurate frequency steps over the course of the laser scan. Files are processed by a program called *et.f*, which uses free spectral range of the etalon cavity (FSR = 250.51 MHz) in the interpolation. Afterward, these files are fit to a Voigt line shape function, where "a" and "b" files are processed by programs *voigta.f* and *voigtb.f*, respectively. These routines extract Gaussian and Lorentzian widths, and also calculate the area under each profile. Each parameter is stored in the header of the output file, which are listed in Table 2.3 for vscan*date*b.*xxx* files. The integrated areas are tabulated as column integrated densities for each transition. These values are then fit to the two-temperature Boltzmann model in a program called *logalpha.f*. Extracted values of α and $T_{rot}(IS)$ are then used to refit the absorption profiles with a two-temperature line shape in a program called *voigt2.f*. The final step in the Dopplerimetry analysis requires mock line shapes that are generated from the sum of TD and IS components. These curves are calculated in a script called *2temp.pl*, which are then fit to a single Gaussian curve in *gauss.f*. Further details of each program are included in the comments in Appendix E.

References for Chapter II

[1] D. R. Miller, in *Atomic and Molecular Beam Methods*, edited by G. Scoles (Oxford University Press, New York, 1988), Vol. 1, pp. 14.

[2] S. L. Lednovich and J. B. Fenn, *AIChE J.* **23**, 454 (1977).

[3] M. J. Weida, University of Colorado, 1996.

[4] J. T. Verdeyen, *Laser Electronics*, 3rd ed. (Prentice Hall, Upper Saddle River, 2000).

[5] R. E. Simpson, *Introductory Electronics for Scientists and Engineers*, 2nd ed. (Allyn and Bacon, Inc, Boston, 1987).

[6] G. Guelachvili and K. N. Rao, *Handbook of Infrared Standards With Spectral Maps and Transitions Assignments between 3 and 2600 microns.* (Academic Press, Inc., London, 1986).

[7] J. W. C. Johns, *J. Molecular Spectroscopy* **134**, 433 (1989).

[8] D. Kaur, A. M. Desouza, J. Wanna, S. A. Hammad, L. Mercorelli, and D. S. Perry, *Appl. Opt.* **29**, 119 (1990).

[9] W. B. Chapman, University of Colorado, 1997.

[10] D. Proch and T. Trickl, *Rev. Sci. Instrum.* **60**, 713 (1989).